TECHNISCHE UNIVERSITÄT WIEN
Vienna University of Technology

Diplomarbeit

Impact of Construction Faults on In Situ Airborne Sound Insulation of Noise Barriers

Ausgeführt am

Institut für Angewandte Physik der Technischen Universität Wien

unter der Anleitung von

Ao.Univ.Prof. Dipl.-Ing. Dr.techn. Martin Gröschl

in Zusammenarbeit mit dem

Austrian Institute of Technology, Mobility Department

durch

Martin Pfister

Braitnerstr. 20A/3

2500 Baden

7. August 2014 _____

Acknowledgements

I want to express my gratitude to Univ.Prof. Dr. Martin Gröschl for his support in writing this thesis.

I am grateful to Dott. Ing. Marco Conter for his offer to write this thesis in cooperation with the Austrian Institute of Technology. My thanks go to my colleagues at the AIT, in particular to

- Dipl.-Ing. Reinhard Wehr for his valuable insight into acoustic measurements,
- Dipl.-Ing. Paul Reiter for his advice concerning the simulations,
- Martin Czuka, Dr. Martin Kriegisch and Dr. Sara Gasparoni for their general willingness to share their experience and
- Dipl.-Ing. Rainer Stütz and Dipl.-Ing. Simon Breuss for allowing me to use the computation server even though that sometimes implied delays for their own calculations.

Kurzfassung

Eine der größten Lärmquellen stellt der stetig zunehmende Straßenverkehr dar. Um die Beeinträchtigung der in der Nähe von Hauptverkehrsachsen lebenden Bevökerung trotzdem möglichst gering zu halten, werden oft Lärmschutzmaßnahmen wie z.B. das Errichten von Lärmschutzwänden durchgeführt. Die Beurteilung dieser Lärmschutzmaßnahmen ist durch verschiedene Normen geregelt; so befasst sich die Normenreihe EN 1793 beispielsweise mit „Lärmschutzvorrichtungen an Straßen – Prüfverfahren zur Bestimmung der akustischen Eigenschaften".

Die dieser Diplomarbeit zugrunde liegende Fragestellung ist die nach den Auswirkungen von Einbaufehlern auf die akustischen Eigenschaften von Lärmschutzwänden. Typische Einbaufehler sind horizontale Spalte, die zwischen Boden und Lärmschutzwand oder zwischen einzelnen Elementen frei bleiben, oder Löcher, die auf Beschädigungen der Ecken der Elemente vor der Montage zurückzuführen sein können.

Die Schalltransmission durch diese Fehlstellen in Lärmschutzwänden wird numerisch und experimentell betrachtet. Zur numerischen Berechnung wird die für nach außen unbeschränkte Problemstellungen besonders geeignete Randelementemethode (BEM, boundary element method) verwendet. Im experimentellen Teil werden an einem Lärmschutzwandprüfstand Messungen nach der Norm EN 1793-6 (aus dem EU-Projekt Adrienne) durchgeführt. Abschließend werden die experimentell und numerisch ermittelten Werte mit analytischen Berechnungen nach dem Modell von Gomperts [14] verglichen.

Abstract

The steadily increasing amount of traffic constitutes one of the largest noise sources in the environment. To keep the annoyance for people living close to heavily used roads as low as possible, noise reduction measures such as the erection of noise barriers are often taken. The assessment of these noise reduction measures is regulated by a number of standards; the series EN 1793 for instance covers the topic "Road traffic noise reducing devices – Test method for determining the acoustic performance".

The problem forming the basis of this master's thesis is the impact of construction faults on the acoustic properties of noise barriers. Typical construction faults are horizontal gaps that remain open between individual elements or holes that result through damages to the corners of elements prior to the installation.

The sound transmission through these faults in noise barriers is examined numerically and experimentally. For the numerical treatment the boundary element method (BEM) that is especially suited for externally unconfined problems is used. The experimental part consists of measurements according to the standard EN 1793-6 (from the EU project Adrienne) that are carried out at a noise barrier test facility. Finally the results obtained from the simulations and the measurements are compared with calculations according to the analytical model by Gomperts [14].

Contents

1 Introduction

Cars and other convenient means of transport enable people to cover great distances in reasonable time, but at the same time bring about new problems like increased noise pollution. Of course the most reasonable way of dealing with noise is reducing its emission, but where this is not sufficiently possible, trying to shield off noise by building barriers is a strategy commonly employed.

Most noise barriers follow a simple design principle: Acoustic elements are stacked on each other and held in position by posts. This makes them rather easy to build: At the construction site it is sufficient to make a deep foundation for the posts every couple of metres and then insert the acoustic elements in between from above. Unfortunately, this simple construction can lead to small gaps or holes to appear and let noise leak through the barrier.

Figure 1.1: Train track with noise barriers

Generally speaking, the effectivity of noise barriers is limited by the following properties [16]:

- The sound insulation of the elements – how much noise is transmitted through the barrier,
- the height of the barrier and the geometry at the top – how much sound is diffracted over the barrier,
- the reflection properties – reflections increase the noise levels at the opposite side of the road,
- the positions of the sources – lower sources (e.g. tyres) are shielded better than higher sources (e.g. the pantograph of a train).

The aim of this thesis is to study the influence of gaps on the actual sound insulation.

In the following pages photos of three kinds of gaps are presented: Figure 1.2 shows a gap between the base element of a barrier and one of the acoustic elements. Usually a rubber band would seal this gap, but in this case the rubber band hangs out of the barrier and the gap remains wide open. The next figure shows a case where the gap is not the result of careless execution at the construction site, but part of a bad design: The gap in figure 1.3 remains open, because the acoustic elements sit on top of the feet of the posts through which the posts are screwed on to the concrete base. Figure 1.4 shows holes in a barrier next to the foot of a post. Even though the design of this barrier is superior to the previous one, a significant gap is still left open. (The noise barriers shown in figures 1.2–1.4 were built in 2011.)

Figure 1.2: Gap between noise barrier elements

Figure 1.3: Gap underneath a noise barrier

Figure 1.4: Holes around the base of the post

2 Theoretical Background

2.1 Introduction

Acoustics is the science that studies sound, its origin, propagation and perception. The term "sound" denotes mechanical vibrations of an elastic medium that spread out as sound waves in gases, liquids and solids. For this thesis, only sound waves in air and within the frequency range of human hearing, which is approximately from 20 Hz to 20 kHz, are of interest.

Sound waves can be characterised as small variations of the state variables pressure p, density ρ of the media and displacement velocity $\vec{v}$ of the particles. The total values $p_{tot}(\vec{r}, t)$, $\rho_{tot}(\vec{r}, t)$ and $\vec{v}_{tot}(\vec{r}, t)$ are the superimpositions of the static quantities without any sound field p_0, ρ_0 and $\vec{v}_0$ and the alternations due to the sound field $p(\vec{r}, t)$, $\rho(\vec{r}, t)$ and $\vec{v}(\vec{r}, t)$:

$$p_{tot}(\vec{r}, t) = p_0 + p(\vec{r}, t) \tag{2.1}$$

$$\rho_{tot}(\vec{r}, t) = \rho_0 + \rho(\vec{r}, t) \tag{2.2}$$

$$\vec{v}_{tot}(\vec{r}, t) = \vec{v}_0 + \vec{v}(\vec{r}, t) = \vec{v}(\vec{r}, t) \tag{2.3}$$

$\vec{v}_0$ does not depend on the time t or the position $\vec{r}$, therefore it is always possible to choose the coordinate system so that $\vec{v}_0 = 0$.

2.2 Basic Equations

2.2.1 Adiabatic Equation of State

The changes of the state variables in sound waves usually occur fast enough that they do not involve heat transfer and are thus adiabatic. The equation describing a reversible adiabatic process in a gas is

$$p \cdot V^{\kappa} = \text{constant} \tag{2.4}$$

with the adiabatic index $\kappa = \frac{C_p}{C_V}$ being the ratio of the heat capacity at constant pressure C_p to the heat capacity at constant volume C_V. Substituting $V = \frac{m}{\rho}$, we can apply equation 2.4 both to the static quantities p_0, ρ_0 without sound field and the total quantities p_{tot}, ρ_{tot} that include the sound field, thus arriving at

$$p_{tot}\frac{m^\kappa}{{\rho_{tot}}^\kappa} = p_0\frac{m^\kappa}{{\rho_0}^\kappa}. \tag{2.5}$$

Moving all pressure variables to one side and the density variables to the other and applying Taylor series up to the linear term, we get a relation between the relative sound pressure $\frac{p}{p_0}$ and the relative sound density $\frac{\rho}{\rho_0}$:

$$\frac{p_{tot}}{p_0} = \left(\frac{\rho_{tot}}{\rho_0}\right)^\kappa = \tag{2.6}$$

$$= \frac{p_0 + p}{p_0} = 1 + \frac{p}{p_0} = \left(1 + \frac{\rho}{\rho_0}\right)^\kappa = 1 + \kappa \cdot \frac{\rho}{\rho_0} + \mathcal{O}\left(\left(\frac{\rho}{\rho_0}\right)^2\right) \tag{2.7}$$

Neglecting the higher-order terms yields

$$\frac{p}{p_0} = \kappa\frac{\rho}{\rho_0}. \tag{2.8}$$

Solving equation 2.8 for the sound pressure p leads to the relation

$$p = \rho \cdot \kappa\frac{p_0}{\rho_0}, \tag{2.9}$$

where the constant $c = \sqrt{\kappa\frac{p_0}{\rho_0}}$ can be defined. Later on the wave equation will show that c is the speed of sound in air. The acoustic version of the adiabatic equation of state can now be written as

$$\boxed{p = \rho c^2.} \tag{2.10}$$

2.2.2 Euler's Law of Compression

The theoretical foundation of acoustics in gases is given by Euler's equations of fluid dynamics. The first equation results from the following consideration: The amount of mass that leaks from the volume V through its surface ∂V in the time $\mathrm{d}t$ equals the change of mass in the volume V:

$$dt \oint_{\partial V} \rho_{tot}\,\vec{v}_{tot}\,\mathrm{d}\vec{A} = -dt\frac{\partial}{\partial t}\int_V \rho_{tot}\,\mathrm{d}V \tag{2.11}$$

Applying Gauss's divergence theorem $\oint_{\partial V} \vec{F}\, \mathrm{d}\vec{A} = \int_V \nabla \cdot \vec{F}\, \mathrm{d}V$ to the left hand side and comparing the integrands yields **Euler's law of compression**:

$$\nabla \cdot (\rho_{tot}\, \vec{v}_{tot}) + \frac{\partial \rho_{tot}}{\partial t} = 0 \tag{2.12}$$

Inserting equations 2.2 and 2.3 and, to improve clarity, writing out the time and spatial dependences produces

$$\nabla \cdot [\rho_0\, \vec{v}(\vec{r}, t)] + \underbrace{\nabla \cdot [\rho(\vec{r}, t)\, \vec{v}(\vec{r}, t)]}_{\approx 0} + \underbrace{\frac{\partial \rho_0}{\partial t}}_{=0} + \frac{\partial \rho(\vec{r}, t)}{\partial t} = 0. \tag{2.13}$$

The second term in equation 2.13 contains the quadratic product of the sound density and the displacement velocity and therefore is small enough to neglect and the third term is zero because ρ_0 is constant in time. We thus arrive at the **acoustic law of compression**:

$$\rho_0 \nabla \cdot \vec{v} + \frac{\partial \rho}{\partial t} = 0 \tag{2.14}$$

Using the relation $p = \rho c^2$ from equation 2.10, we can also write

$$\boxed{\rho_0 \nabla \cdot \vec{v} + \frac{1}{c^2} \frac{\partial p}{\partial t} = 0.} \tag{2.15}$$

2.2.3 Euler's Law of Inertia

The second equation of fluid dynamics is along the lines of Newton's second law $\vec{F} = m \frac{\mathrm{d}\vec{v}}{\mathrm{d}t}$ that says that the force on an object is equal to its mass times its acceleration, but adds another term that accounts for the pressure gradients. For the illustration of this second term take a cube with side lengths $\mathrm{d}x$, $\mathrm{d}y$, $\mathrm{d}z$ as depicted in figure 2.1 and consider the forces in direction x only. The force on the left side of the cube is $p_{tot}(x)\, \mathrm{d}y\, \mathrm{d}z$ and the force on the right side is $-p_{tot}(x + \mathrm{d}x)\, \mathrm{d}y\, \mathrm{d}z$:

$$p_{tot}(x)\, \mathrm{d}y\, \mathrm{d}z - p_{tot}(x + \mathrm{d}x)\, \mathrm{d}y\, \mathrm{d}z = \frac{p_{tot}(x) - p_{tot}(x + \mathrm{d}x)}{\mathrm{d}x}\, \mathrm{d}x\, \mathrm{d}y\, \mathrm{d}z = -\frac{\partial p_{tot}}{\partial x}\, \mathrm{d}x\, \mathrm{d}y\, \mathrm{d}z \tag{2.16}$$

Still accounting for forces along the x-axis only, the full equation becomes:

$$\rho_{tot} \frac{\mathrm{d}v_{tot,x}}{\mathrm{d}t} + \frac{\partial p_{tot}}{\partial x} = F_x \tag{2.17}$$

Adding the corresponding terms for directions y and z yields **Euler's law of inertia**:

$$\rho_{tot} \frac{\mathrm{d}\vec{v}_{tot}}{\mathrm{d}t} + \nabla p_{tot} = \vec{F} \tag{2.18}$$

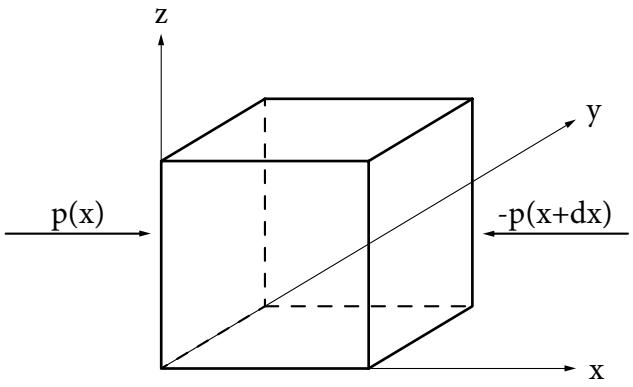

Figure 2.1: Illustration for the derivation of Euler's law of inertia

The total differential $\frac{\mathrm{d}\vec{v}_{tot}}{\mathrm{d}t}$ in equation 2.18 can be calculated using the chain rule. Again taking only the values in x direction at first leads to

$$\begin{aligned}\frac{\mathrm{d}v_{tot,x}}{\mathrm{d}t} &= \frac{\partial v_{tot,x}}{\partial t} + \frac{\partial v_{tot,x}}{\partial x}\frac{\mathrm{d}x}{\mathrm{d}t} + \frac{\partial v_{tot,x}}{\partial y}\frac{\mathrm{d}y}{\mathrm{d}t} + \frac{\partial v_{tot,x}}{\partial z}\frac{\mathrm{d}z}{\mathrm{d}t} \\ &= \frac{\partial v_{tot,x}}{\partial t} + \left(\frac{\mathrm{d}\vec{r}}{\mathrm{d}t}\cdot\nabla\right) v_{tot,x} = \frac{\partial v_{tot,x}}{\partial t} + \left(\vec{v}_{tot}\cdot\nabla\right) v_{tot,x}.\end{aligned} \tag{2.19}$$

In three dimensions the relation becomes

$$\frac{\mathrm{d}\vec{v}_{tot}}{\mathrm{d}t} = \frac{\partial \vec{v}_{tot}}{\partial t} + \left(\vec{v}_{tot}\cdot\nabla\right)\vec{v}_{tot}. \tag{2.20}$$

Hence the total acceleration $\frac{\mathrm{d}\vec{v}_{tot}}{\mathrm{d}t}$ can be viewed as the sum of the local acceleration $\frac{\partial\vec{v}_{tot}}{\partial t}$ and the convective acceleration $\left(\vec{v}_{tot}\cdot\nabla\right)\vec{v}_{tot}$. Assuming no convection and freedom of forces $\vec{F} = 0$ yields

$$\rho_{tot}\frac{\partial\vec{v}_{tot}}{\partial t} + \nabla\, p_{tot} = 0. \tag{2.21}$$

Again inserting equations 2.2 and 2.3 and writing out the time and spatial dependences produces

$$\rho_0\frac{\partial\vec{v}(\vec{r},t)}{\partial t} + \underbrace{\rho(\vec{r},t)\frac{\partial\vec{v}(\vec{r},t)}{\partial t}}_{\approx 0} + \underbrace{\nabla\, p_0}_{=0} + \nabla\, p(\vec{r},t) = 0. \tag{2.22}$$

The second term is negligible because it is quadratic and the third term is zero because p_0 is constant in space. We thus arrive at the acoustic law of inertia:

$$\boxed{\rho_0\frac{\partial\vec{v}}{\partial t} + \nabla\, p = 0} \tag{2.23}$$

2.2.4 Wave Equation

Taking the acoustic law of compression from equation 2.15 and calculating the time derivative yields

$$\frac{1}{c^2}\frac{\partial^2 p}{\partial t^2} + \rho_0 \nabla \cdot \frac{\partial \vec{v}}{\partial t} = 0. \tag{2.24}$$

Solving the acoustic law of inertia from equation 2.23 for $\frac{\partial \vec{v}}{\partial t}$ results in

$$\frac{\partial \vec{v}}{\partial t} = -\frac{1}{\rho_0} \nabla p. \tag{2.25}$$

Inserting equation 2.25 into equation 2.24 results in the **wave equation**

$$\boxed{\frac{1}{c^2}\frac{\partial^2 p}{\partial t^2} - \nabla^2 p = 0.} \tag{2.26}$$

2.3 Sound Pressure Level and Frequency Bands

The range of sound pressure values from the human threshold of audibility ($\sim 2 \times 10^{-5}$ Pa at 1 kHz) to the threshold of pain (~ 20 Pa) is about six magnitudes. Additionally, the human perception of loudness is logarithmic; a change of the sound pressure to the double will be perceived as the same change of loudness independent of the starting sound pressure. It is thus impractical to use the sound pressure values directly to indicate how loud a certain sound wave is perceived. Instead, the logarithmic sound pressure level L_p has been defined as

$$L_p = 10 \log_{10}\left(\frac{{p_{\text{rms}}}^2}{{p_0}^2}\right) = 20 \log_{10}\left(\frac{p_{\text{rms}}}{p_0}\right) \qquad \text{with } p_0 = 2 \times 10^{-5}\,\text{Pa}. \tag{2.27}$$

The quantity p_{rms} denotes the root mean square of the acoustic pressure p with T the length of one period:

$${p_{\text{rms}}}^2 = \frac{1}{T}\int_0^T p^2(t)\,\mathrm{d}t. \tag{2.28}$$

The unit for the sound pressure level is 1 decibel = 1 dB; the range mentioned above thus becomes an easier to grasp 0–120 dB.

The perceived loudness of a sound source depends on a lot of factors in addition to the sound pressure, the greatest of which is the frequency composition of the signal. The most

commonly used means to get a single-number value for the loudness of a signal is by applying an A-weighting filter. The A-weighting curve is defined in the international standard IEC 61672 [30] and is roughly equal to the inverted human threshold of audibility.

The frequency perception of the human hearing is logarithmic, for example a doubling of the frequency will be perceived as an equal change in pitch disregarding the starting frequency. For analysing a signal it can be useful to split the frequency range in question into several smaller bands. The convention is to use either *octave bands* (lower frequency limit to upper frequency limit $f_l : f_u = 1 : 2$) or *third octave bands* ($f_l : f_u = 1 : \sqrt[3]{2}$) and start with a band centre frequency $f_c = \sqrt{f_l f_u}$ of 1000 Hz.

2.4 Signal Processing

2.4.1 LTI Systems

An *acoustic system* is formed by a sound source, a sound receiver and the sound path from the source to the receiver. The sound source, for example a passing car or for measurement purposes a loudspeaker, can be described as the excitation or input signal $x(t)$. The output signal $y(t)$ of the system is the sound heard by neighbours or recorded by a measurement microphone. The sound path is then described by the operator L:

$$y(t) = \mathrm{L}\{x(t)\} \tag{2.29}$$

An acoustic system can be linear or non-linear. Linearity means that the principle of superposition applies: The net response caused by two stimuli is equal to the sum of the responses which would have been caused by each of the stimuli individually:

$$\mathrm{L}\{a_1 x_1(t) + a_2 x_2(t)\} = a_1 \mathrm{L}\{x_1(t)\} + a_2 \mathrm{L}\{x_2(t)\} \tag{2.30}$$

with $x_1(t)$ and $x_2(t)$ being two independent signals and a_1 and a_2 two arbitrary constants.

A system is referred to as time invariant, if the only change of the output by time shifting the input is an equal shift of time:

$$y(t) = \mathrm{L}\{x(t)\} \quad \Leftrightarrow \quad y(t-\tau) = \mathrm{L}\{x(t-\tau)\} \tag{2.31}$$

Airborne acoustic systems with a constant temperature, no wind and sound pressure levels low enough that they are not harmful to human hearing can be assumed to be both *linear* and *time-invariant*.

2.4.2 Impulse Responses

Any signal $x(t)$ can be written as the convolution of the signal itself with the Dirac delta:

$$x(t) = \int_{-\infty}^{\infty} x(\tau)\,\delta(t-\tau)\,\mathrm{d}\tau. \tag{2.32}$$

Applying the operator L of an LTI system yields

$$\begin{aligned} y(t) &= \mathrm{L}\{x(t)\} \\ &= \mathrm{L}\left\{\int_{-\infty}^{\infty} x(\tau)\,\delta(t-\tau)\,\mathrm{d}t\right\} \\ &= \int_{-\infty}^{\infty} x(\tau)\,\underbrace{\mathrm{L}\{\delta(t-\tau)\}}_{h(t-\tau)}\,\mathrm{d}t. \end{aligned} \tag{2.33}$$

Hence an impulse response is a sufficient description of an LTI system:

$$h(t) = \mathrm{L}\{\delta(t)\} \tag{2.34}$$

To calculate the impulse response, the function $x_a(t)$ that satisfies the equation

$$h(t) = \int_{-\infty}^{\infty} x_a(t-\tau)y(\tau)\,\mathrm{d}\tau, \tag{2.35}$$

that is the convolution of $x_a(t)$ with the output $y(t)$, produces the impulse response. Considerations in the frequency space (see for example [8]) show that if the spectrum of the system input $x(t)$ is similar to that of white noise, meaning its spectral density is constant, the function $x_a(t)$ is equal to the time reverse of the system input:

$$x_a(t) = x(-t) \tag{2.36}$$

Hence the impulse response is the convolution of the output signal with the time-reversed input signal:

$$h(t) = \int_{-\infty}^{\infty} x(\tau-t)y(\tau)\,\mathrm{d}\tau \tag{2.37}$$

2.4.3 Fourier Transform

The Fourier transform produces the frequency spectrum of a signal $x(t)$:

$$X(f) = \int_{-\infty}^{\infty} x(t)\, e^{-\mathrm{i}2\pi f t}\, \mathrm{d}t. \tag{2.38}$$

In digital signal processing any signal is represented by a finite number of time-discrete values; it is therefore necessary to replace the integral with a sum. To calculate the frequency spectrum of a discrete signal $x[n]$, the discrete Fourier transform (DFT) can be used:

$$X[k] = \sum_{n=0}^{N-1} x[n]\, e^{-\mathrm{i}\,2\pi \frac{nk}{N}}, \tag{2.39}$$

with the frequency index k and the sample index n both going from 0 to $N-1$. The inverse discrete Fourier transform (IDFT) is

$$x[n] = \frac{1}{N} \sum_{n=0}^{N-1} X[k]\, e^{\mathrm{i}\,2\pi \frac{nk}{N}}. \tag{2.40}$$

For real sample values $x[n]$ the second half of the complex spectrum $X[k]$ is equal to the reversed and conjugate-complex first half:

$$x[n] \in \mathbb{R}\ \forall\ n \quad \Leftrightarrow \quad X[k] = X^*[N-k] \tag{2.41}$$

The other direction is true as well: A real spectrum $X[k]$ corresponds to complex sample values $x[n]$ for which holds

$$X[k] \in \mathbb{R}\ \forall\ k \quad \Leftrightarrow \quad x[n] = x^*[N-n]. \tag{2.42}$$

Although most measurements produce only sound pressure amplitude information, results obtained from computer simulations are complex numbers and contain both amplitude and phase of the sound pressure. These complex sound pressure values together with the relation in equation 2.41 will be used later on to calculate a real signal from the simulations.

2.4.4 Maximum Length Sequences and Hadamard Transform

A maximum length sequence (MLS) is a pseudorandom binary sequence, that means it has a frequency spectrum equal to white noise and it only contains the two amplitude states 0 and 1. It can be generated using a linear feedback shift register (LFSR). If the LFSR

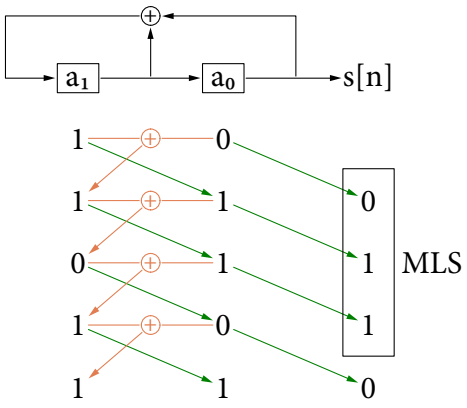

Figure 2.2: Linear feedback shift register of length 2 that generates a maximum length sequence of length $2^2 - 1 = 3$

is of length n, the generated MLS will be of length $2^n - 1$ and will be repeated afterwards. Figure 2.2 gives an example of an LFSR of length 2 generating an MLS of length 3.

An MLS is especially suited as a test input signal, because there is a fast algorithm for the convolution of an MLS with a signal. Because in digital signal processing one uses discrete functions, the calculation of the impulse response (equation 2.37) becomes

$$h[t] = \sum_{\tau=0}^{N-1} x[\tau - t]\, y[\tau]\,. \tag{2.43}$$

The calculation can be seen as a matrix-vector-multiplication of the MLS matrix x and the system output y. The MLS matrix contains the MLS in the first line and cyclic permutations in the subsequent lines. Using only simple operations, the MLS matrix can be converted to the HADAMARD matrix. A HADAMARD matrix is a quadratic matrix of the size 2^mx2^m with m an integer. The HADAMARD matrix of order m can be constructed using the following rule:

$$H_0 = 1, \qquad H_m = \begin{pmatrix} H_{m-1} & H_{m-1} \\ H_{m-1} & -H_{m-1} \end{pmatrix} \tag{2.44}$$

For the multiplication of the HADAMARD matrix with another vector, there is a fast algorithm called the fast HADAMARD transform (FHT) similar to the fast FOURIER transform that produces the same result as the matrix-vector-multiplication in less time. The FHT is a divide and conquer algorithm that takes advantage of the symmetries and antisymmetries in the HADAMARD matrix and recursively breaks down the HADAMARD transform into smaller, similar operations. To convert an MLS matrix to the matching HADAMARD matrix, one needs to add a column and a line containing only zeros, then replace all ones

with minus ones and all zeros with ones ($1 \to -1$, $0 \to 1$) and apply the suitable row and column interchanges. It is computationally more efficient to interchange the appropriate rows of the measured system output y, apply the FHT, interchange the suitable columns and multiply with a scaling factor than to directly calculate the matrix-vector-product in equation 2.43. When using an MLS as test signal, the MLS usually is played back multiple times and the impulse response is then calculated for each time. Averaging over multiple impulse responses improves the signal-to-noise-ratio, because the noise is a stochastic signal not correlated to the impulse response; doubling the number of impulse responses increases the signal-to-noise-ration by 3 dB [29]. If the aim of a measurement is to get a FOURIER spectrum, it is not possible to directly calculate the FFT from the output of the system, because the length of the MLS is $2^n - 1$, but the COOLEY–TUKEY FFT algorithm, which is the most commonly used FFT algorithm, needs an input of length 2^n. Zero-padding the measured signal leads to an error, but calculating the impulse response first and append a zero then is a valid approach to get a length suitable for the FFT.

2.5 Boundary Element Method (BEM)

While analytical solutions exist for some scattering problems, most complicated geometries demand numerical techniques to find approximate solutions. The most common method for solving partial differential equations is the finite element method (FEM) that works by discretising the whole volume. For externally unconfined problems though it is impossible to discretise the whole, infinite volume; therefore FEM needs an additional strategy like perfectly matched layers (PML) that allows the truncation of the computational region without adding reflections from the borders. Another method, the boundary element method (BEM), is better suited for externally unconfined problems, because it only requires discretisation of the surface of the scattering object. The mathematical background to the BEM will be described in this chapter.

2.5.1 HELMHOLTZ Equation

In chapter 2.2.4 wave equation 2.26 was derived:

$$\nabla^2 p - \frac{1}{c^2}\frac{\partial^2 p}{\partial t^2} = 0. \tag{2.45}$$

Assuming time-harmonic waves $p(\vec{r}, t) = \mathrm{Re}\left\{p(\vec{r})\, e^{\mathrm{i}\omega t}\right\}$, the wave equation reduces to the HELMHOLTZ equation

$$\boxed{\nabla^2 p + k^2 p = 0} \tag{2.46}$$

with the spatial dependencies and the time factor $e^{i\omega t}$ omitted and using the wave number $k = \frac{\omega}{c}$ and the circular frequency $\omega = 2\pi f$.

A point source or acoustic monopole is a mathematical abstraction that is extremely useful for describing acoustic problems. A point source is an appropriate approximation of a source of a size much smaller than a wavelength. It can be thought of as the limiting case of a pulsating sphere where the radius tends to zero. Most loudspeakers used for acoustic measurements are designed to have a spherical directional characteristic.

The Green's function is the fundamental solution to the Helmholtz equation. It is the solution to the inhomogeneous equation with a point source represented by the Dirac delta distribution on the right hand side:

$$(\nabla^2 + k^2)\, G(\vec{r}_0, \vec{r}) = -\delta(\vec{r}_0 - \vec{r}). \tag{2.47}$$

The free-space Green's function in three dimensions is

$$G(\vec{r}_0, \vec{r}) = \frac{e^{-ik|\vec{r}_0 - \vec{r}|}}{4\pi|\vec{r}_0 - \vec{r}|}. \tag{2.48}$$

2.5.2 Sommerfeld's Radiation Condition

In order to solve the Helmholtz equation, it is necessary to specify a boundary condition at infinity. The reason for doing so is to make sure that all sources are energy sources and not sinks, that energy from these sources scatters to infinity and that no energy is radiated from infinity. A solution to the Helmholtz equation that satisfies these conditions is called radiating. For time-harmonic waves in three dimensions Sommerfeld's radiation condition can be written as

$$\lim_{r\to\infty}\left[r\left(\frac{\partial p}{\partial r} + ikp\right)\right] = 0. \tag{2.49}$$

2.5.3 Helmholtz Integral Equation

The following development starts with the identity

$$G\,(\nabla^2 + k^2)\, p - p\,(\nabla^2 + k^2)\, G = \nabla \cdot (G\nabla p - p\nabla G), \tag{2.50}$$

which may be shown to be true by simply expanding the terms. Equation 2.50 is valid in the volume V that has two surfaces: The inner surface S is the one relevant for our calculations and the outer surface S_∞ faces infinity (see figure 2.3).

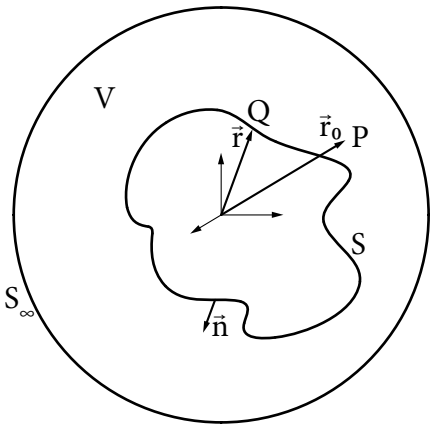

Figure 2.3: Sketch of the volume V, the surfaces S and S_∞ and the points P and Q

Integrating equation 2.50 over the volume V and applying Gauss's divergence theorem to the right hand side yields

$$\int_V G \underbrace{(\nabla^2 + k^2)\, p}_{=0}\, \mathrm{d}V - \underbrace{\int_V p\,(\nabla^2 + k^2)\, G\, \mathrm{d}V}_{=C(\vec{r}_0)\, p(\vec{r}_0)} = -\int_S (G\nabla p - p\nabla G)\, \vec{n}\, \mathrm{d}S + \underbrace{I_{S_\infty}}_{=0}, \quad (2.51)$$

where $\vec{n}$ is the unit vector perpendicular to S pointing into V. The first integral in equation 2.51 is zero because Helmholtz equation 2.46 is valid in all of V. Concerning the second integral, writing out all spacial dependencies and applying the definition of Green's function (equation 2.47) results in

$$-\int_V p(\vec{r})\,(\nabla^2 + k^2)\, G(\vec{r}_0, \vec{r})\, \mathrm{d}V = C(\vec{r}_0)\, p(\vec{r}_0) \quad (2.52)$$

with the factor

$$C(\vec{r}_0) = \begin{cases} 0 & \text{for } \vec{r}_0 \text{ inside } S \\ 1 & \text{for } \vec{r}_0 \text{ outside } S \\ \frac{1}{2} & \text{for } \vec{r}_0 \text{ on } S \text{ if } S \text{ is planar at } \vec{r}_0. \end{cases} \quad (2.53)$$

The remaining terms of equation 2.51, i.e. the terms on the right hand side of the equation, are two integrals, one over the inner surface S and one over the outer surface S_∞. Assuming S_∞ to be a sphere of radius r_{S_∞}, the integral over S_∞ is the only term that depends on r_{S_∞} and therefore the integral I_{S_∞} needs to be constant. It can be shown that because of Sommerfeld's radiation condition $I_{S_\infty} = 0$ (see e.g. [8]).

The Helmholtz integral equation can thus be rewritten as

$$C(\vec{r}_0)\, p(\vec{r}_0) = \int_S \left(-G(\vec{r}_0, \vec{r}) \frac{\partial p(\vec{r})}{\partial n} + p(\vec{r}) \frac{\partial G(\vec{r}_0, \vec{r})}{\partial n} \right) \mathrm{d}S \tag{2.54}$$

The case examined in this thesis is a scattering problem: A point source emits sound waves that get scattered by a body with a rigid surface. One possible way to mathematically deal with the point source would be to change the Green's function, but the strategy employed here is a different one: The pressure field is split up into two separate fields, one representing the incoming field without any scattering bodies and one representing the scattered field:

$$p = p^{in} + p^{sc}. \tag{2.55}$$

The scattered field p^{sc} does not take the source into account and therefore satisfies the homogeneous Helmholtz equation 2.46. The Helmholtz integral equation for the scattered field p^{sc} therefore is

$$C(\vec{r}_0)\, p^{sc}(\vec{r}_0) = \int_S \left(-G(\vec{r}_0, \vec{r}) \frac{\partial p^{sc}(\vec{r})}{\partial n} + p^{sc}(\vec{r}) \frac{\partial G(\vec{r}_0, \vec{r})}{\partial n} \right) \mathrm{d}S \tag{2.56}$$

For the incoming field p^{in} an inhomogeneous Helmholtz equation that considers the point source has to be solved:

$$\nabla^2 p^{in} + k^2 p^{in} = q \qquad \text{with } q = -\hat{q}\, \delta(\vec{r} - \vec{r}_S). \tag{2.57}$$

The vector $\vec{r}_S$ points to the position of the source. The derivation is largely the same as for the homogeneous Helmholtz equation. The only difference is that, assuming that the source is inside the volume V, the first integral in equation 2.51 does not vanish:

$$\int_V G(\vec{r}_0, \vec{r})\, (\nabla^2 + k^2)\, p^{in}(\vec{r})\ \mathrm{d}V = -\hat{q} \int_V G(\vec{r}_0, \vec{r})\, \delta(\vec{r} - \vec{r}_S)\ \mathrm{d}V = -\hat{q}\, G(\vec{r}_0, \vec{r}_S). \tag{2.58}$$

The Helmholtz integral equation for the incoming field p^{in} therefore is

$$C(\vec{r}_0)\, p^{in}(\vec{r}_0) = \int_S \left(-G(\vec{r}_0, \vec{r}) \frac{\partial p^{in}(\vec{r})}{\partial n} + p^{in}(\vec{r}) \frac{\partial G(\vec{r}_0, \vec{r})}{\partial n} \right) \mathrm{d}S + \hat{q}\, G(\vec{r}_0, \vec{r}_S). \tag{2.59}$$

The full Helmholtz integral equation for $p = p^{in} + p^{sc}$ thus equals the sum of equations 2.56 and 2.59:

$$C(\vec{r}_0)\, p(\vec{r}_0) = \int_S \left(-G(\vec{r}_0, \vec{r}) \frac{\partial p(\vec{r})}{\partial n} + p(\vec{r}) \frac{\partial G(\vec{r}_0, \vec{r})}{\partial n} \right) \mathrm{d}S + p^{ff}(\vec{r}_0) \tag{2.60}$$

with $p^{ff}(\vec{r}_0) = \hat{q}\, G(\vec{r}_0, \vec{r}_S)$.

2.5.4 Numerical Implementation

It is convenient to assume that the surface S in equation 2.60 matches the surface of the scattering body. Because the body has a rigid surface, the boundary conditions on S are of the NEUMANN type:

$$\frac{\partial p(\vec{r})}{\partial n} = 0 \qquad \forall \vec{r} \in S \tag{2.61}$$

The first term in the integral of equation 2.60 therefore vanishes.

For the numerical implementation, the surface S is split into N flat panels and the pressure is considered to be constant within each panel (zero order approximation). The pressure can thus be taken out of the integral and the integral evaluated for each panel separately. Calling the points that the vectors $\vec{r}_0$ and $\vec{r}$ point to P and Q, the equation that needs to be evaluated numerically can be written as

$$C(P)\, p(P) = p(Q) \int_S \frac{\partial G(P,Q)}{\partial n}\, \mathrm{d}S + p^{ff}(P). \tag{2.62}$$

Calculating the sound pressure for a microphone point P anywhere in V requires two steps: The first step is to set up a system of equations for the pressure on the surface of the scattering body by putting both P and Q on S. Then the factor $C(P)$ always becomes $\frac{1}{2}$, p becomes an N-dimensional vector containing the sound pressure values at each of the panels, evaluating the integral $\int_S \frac{\partial G(P,Q)}{\partial n}\, \mathrm{d}S$ for all points P and Q results in the NxN matrix H and p^{ff} becomes a vector containing the incident sound pressure values without any scattering body. The resulting system of equations can be written as

$$(H - \frac{1}{2}\mathbb{I})p = -p^{ff} \tag{2.63}$$

and needs to be evaluated for the vector p. Once the sound pressure is known on all panels, the second step is to evaluate equation 2.62 for every microphone point. Because the microphone points are not on but outside of S, $C(P)$ now is 1. If there are M microphone points, the vectors p_M and p_M^{ff} are of dimension M. The NxM matrix H_M is again obtained by evaluating the integral with P one of the M microphone points and Q one of the N nodal points at the panels. The vector containing the sound pressure values at the microphone points can thus be calculated by solving the system of equations

$$p_M = pH_M + p_M^{ff}. \tag{2.64}$$

2.5.5 The Non-Uniqueness Problem

The solution given above breaks down at certain characteristic frequencies. This so-called non-uniqueness problem is a purely mathematical problem inherent to the HELMHOLTZ integral equation and is not the result of a particular numerical implementation. It was shown by SCHENCK [12] that the characteristic frequencies for a given exterior problem with NEUMANN boundary conditions correspond to the eigenfrequencies of the related interior problem with the same body shape and DIRICHLET boundary conditions. In the same paper, SCHENCK proposes a technique to overcome this problem, the Combined HELMHOLTZ Integral Equation Formulation CHIEF. The basis of CHIEF is to introduce a number of additional points inside S where the sound pressure is known to be zero. This yields an over-determined system that can be solved by approximation.

2.6 Analytical formula by GOMPERTS

In his paper published in 1964, GOMPERTS [14] deduced a formula for the sound transmission factor of narrow slit-shaped apertures in walls. Three years later a follow-up paper by GOMPERTS and KIHLMAN [15] included the results of measurements that showed a rather good agreement with GOMPERTS's formula.

The transmission factor q_{sl} is defined as the ratio of the power radiated through the aperture on the receiving side to the power originally fed to the aperture on the source side. For a plane wave falling perpendicularly upon the wall, the transmission factor of a slit-shaped aperture in the middle of a wall was calculated by GOMPERTS to be

$$q_{sl} = \frac{2\beta k \sin^2(kl)}{\left(\frac{\cos^2[k(l+\alpha)]}{\cos^2(k\alpha)} + \frac{k^2\beta^2}{4}\sin^2(kl)\right)^2 - 2\left(\frac{\cos^2[k(l+\alpha)]}{\cos^2(k\alpha)} + \frac{k^2\beta^2}{4}\sin^2(kl)\right) + 1}, \tag{2.65}$$

with β the width of the gap, $k = 2\pi f$ the wave number, l the thickness of the wall and α the end correction (EULER's constant $\gamma' = 0.57722$):

$$\alpha = \frac{\beta}{\pi}\sqrt{\left(\ln\frac{k\beta}{8} + \gamma'\right)^2 + \left(\frac{\pi}{2}\right)^2}. \tag{2.66}$$

The end correction describes the effects of the gap on the sound field in front of the gap. SMITS and KOSTEN [13] explain the idea behind the end correction with the following example: Consider the case of a regularly perforated panel at some distance from a rigid wall. A sound wave falling upon the system can start a vibration and then the system behaves like a mass-spring oscillator with the compressible air behind the panel acting

as the spring and the air moved through the holes as the mass. The kinetic energy of the system is therefore found in the mass of the air directly in the holes, which is given by the cross section of the holes times the thickness of the panel times the density of the air. If one considered the limiting case of an infinitely thin panel, the mass would also tend to zero, which is contradictory to the fact that even for an infinitely thin panel the kinetic energy has to be greater than in the case without any panel at all. Therefore one has to assume that the moved mass of the mass-spring system is greater than the mass directly inside the holes. The length of this imaginary extension of the holes is called the *end correction* and does not depend on the thickness of the panel. GOMPERTS's term for the end correction given in equation 2.66 only depends on the width of the gap β and the frequency $f = k/2\pi$. Naturally, the end correction does not only apply to infinitely thin panels but needs to be taken into account for panels of all thicknesses.

3 Measurement

3.1 European Standard EN 1793-6

The series of standards "Road traffic noise reducing devices", published by the European Committee for Standardization and its national members under the series EN 1793, describes test methods for the acoustic properties of noise barriers. Two parts of this series of standards address sound insulation: EN 1793-2 [25] describes a method for assessing the sound insulation of a barrier in a test bed. The barrier gets mounted between two reverberation rooms, one of which contains a loudspeaker. The sound insulation is determined by comparing the sound pressure levels of the diffuse fields on both sides of the barrier. EN 1793-6 [27] describes a different method that can also be applied in situ: Impulse responses through the barrier are measured and time windowed and the energy compared to equivalent free-field impulse responses.

Figure 3.1: The noise barrier where the measurements have been carried out. The gap shown is the largest one that has been examined (2 cm)

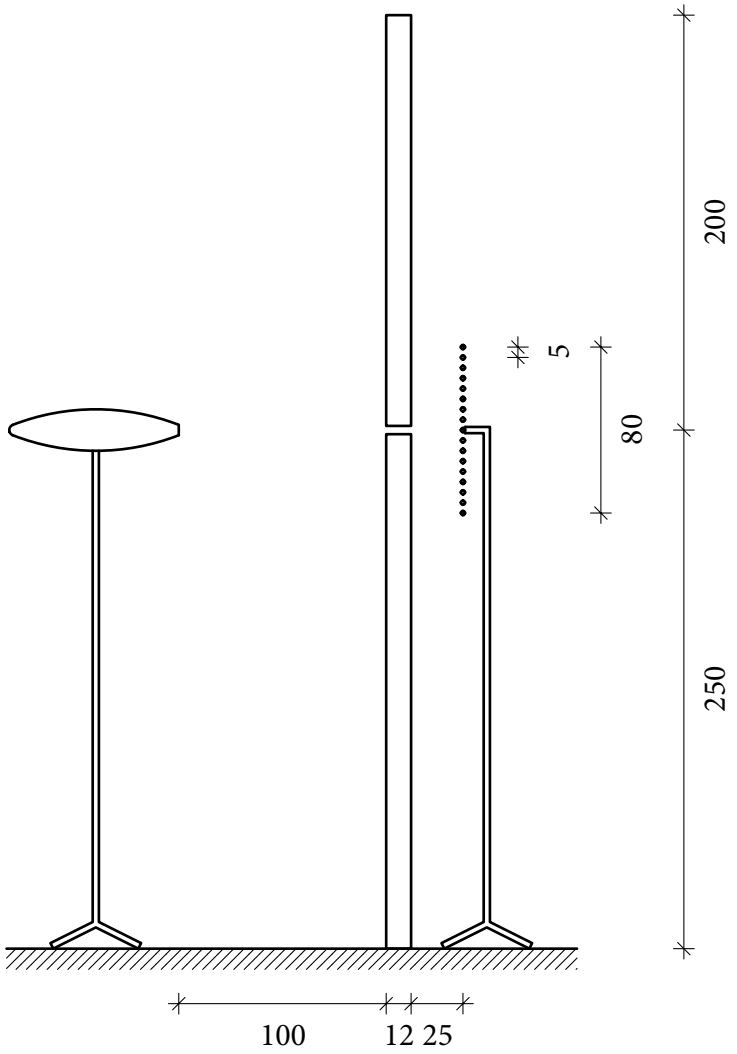

Figure 3.2: Sketch of the measurement setup: Loudspeaker on the left hand side. Noise barrier with a gap in the middle. Dots on the right hand side indicate the microphone positions where the sound pressure was measured for the 2 cm gap. (The standard EN 1793-6 specifies only three different heights for the microphone positions.) Indicated lengths in cm

On the side of the barrier that faces the noise source a loudspeaker is placed at half the barrier's height at a distance of 1 m. To make sure that the components diffracted over the barrier are easy to separate from those transmitted through the barrier, that means to make sure that the lengths of their sound paths are different enough, the barrier needs to be of sufficient height. The standard specifies a minimum barrier height of 4 m for qualification tests. For smaller heights the lower frequency limit below which the results are not reliable increases. On the other side of the barrier nine microphones are placed in a three-by-three grid at a distance of 25 cm from the barrier. The central microphone needs to be at the same height as the loudspeaker and the distance between adjacent microphones should be 40 cm so that the nine positions form a square with a side length of 80 cm. If only one microphone is available, it is also possible to measure the different positions consecutively. The standard rules that an MLS sequence is played back and the impulse responses are calculated from the signal measured by the microphones.

To cancel out any components diffracted over the barrier, a windowing operation on the impulse response is performed in the time domain. The so-called Adrienne window consists of three parts:

- a leading edge of a length of 0.5 ms shaped like the left half of a Blackman-Harris window,
- a flat part of a length of 5.18 ms
- and a trailing edge of 3/7 the length of the main part (that is 2.22 ms) consisting of the right half of a Blackman-Harris window.

The total length of the Adrienne window therefore is 7.9 ms. The Adrienne window should be placed so that the main part starts 0.2 ms prior to the arrival of the direct component peak. The components diffracted around the barrier should not arrive prior to the end of the third part of the Adrienne window. If that is not the case, the second and third part of the Adrienne window have to be shortened accordingly. The arrival times of the direct and the diffracted components should be determined by simple geometric considerations. Figure 3.3B shows the Adrienne window.

To measure the corresponding free-field impulse responses, it is necessary to set up the loudspeaker and the microphones again using the same distances but without the barrier in between. For the free-field impulse responses the same Adrienne window length as for the measurement with the barrier in between has to be applied.

The sound insulation index SI_j in decibels for each frequency band j can be calculated by comparing the energy in the transmitted impulse response to the energy in the free-field

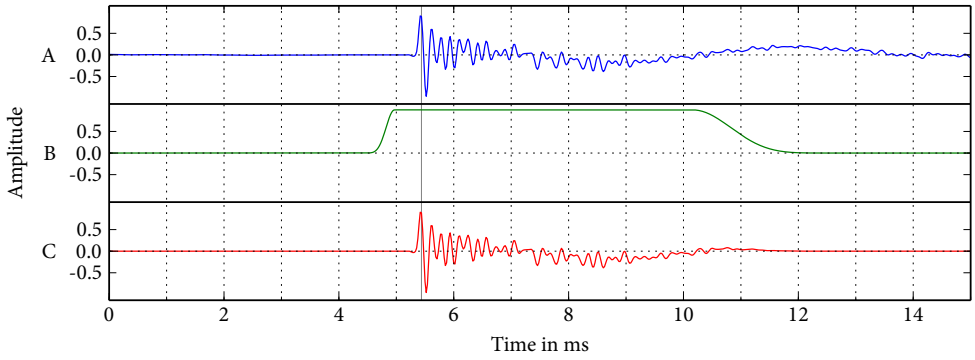

Figure 3.3: Measured impulse responses of the microphone at the centre position. A: Barrier with a 0.4 cm gap. B: Adrienne window. C: Windowed impulse response

impulse response:

$$SI_j = -10\lg\left\{\frac{1}{n}\sum_{k=1}^{n}\frac{\int_{\Delta f_j}|F[h_{tk}(t)w_{tk}(t)]|^2\,\mathrm{d}f}{\int_{\Delta f_j}|F[h_{ik}(t)w_{ik}(t)]|^2\,\mathrm{d}f}\right\} \tag{3.1}$$

$h_{ik}(t)$ and $h_{tk}(t)$ are the incident (free-field) and the transmitted impulse responses and $w_{ik}(t)$ and $w_{tk}(t)$ the corresponding Adrienne windows. F is the symbol of the FOURIER transform, j the index for the third-octave frequency band (between 100 Hz and 5000 Hz), Δf_j the width of the j^{th} band and $n = 9$ the number of microphone points.

Depending on the length of the used Adrienne window, the lower frequency limit has to be determined, so that at least one full wavelength can be accommodated within the Adrienne window. Figure 3.4 shows the lower frequency limit as a function of the height of the noise barrier.

The single-number rating DL_{SI} in decibels is calculated by weighting the sound insulation indices for the different frequency bands with the standardised traffic noise spectrum L_j:

$$DL_{SI} = -10\lg\left(\frac{\sum_{j=m}^{18}10^{0.1L_j}10^{-0.1SI_j}}{\sum_{j=m}^{18}10^{0.1L_j}}\right) \tag{3.2}$$

SI_j is the sound insulation index in the third-octave band j, m the lowest reliable third-octave band (typically the 200 Hz band for a barrier of dimension 4 m × 4 m) and L_j the relative A-weighted sound pressure level of the normalised traffic noise spectrum as defined in EN 1793-3 [26] (see figure 3.5 and table 3.1).

The standard specifies that all measurements have to be done twice, once in the middle of the acoustic elements and once at a post. The global single-number rating of the noise

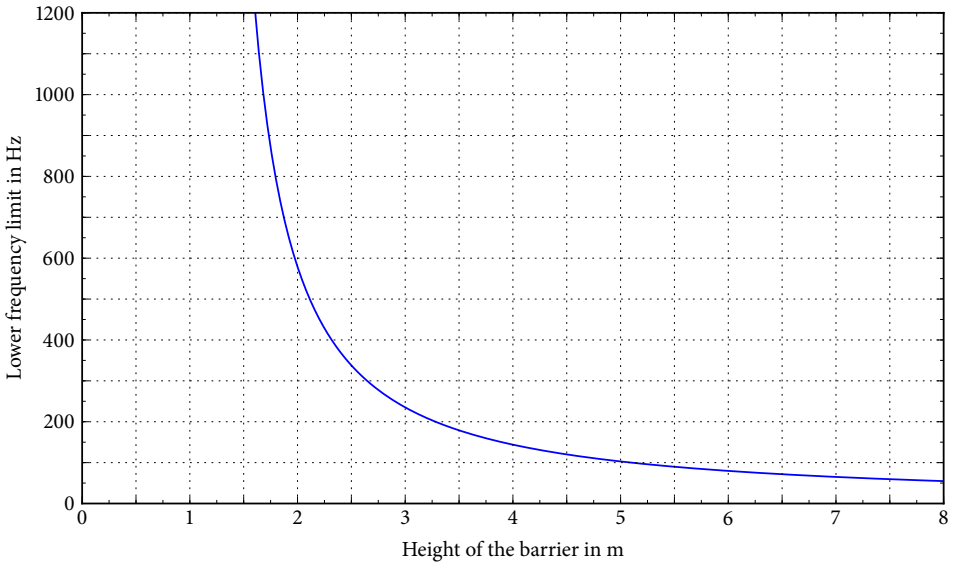

Figure 3.4: Lower frequency limit for sound insulation measurements as a function of the height of the noise barrier

barrier is then calculated by logarithmically averaging the two single-number ratings at the acoustic elements and at the post.

3.2 Measurement Setup

For this thesis a number of measurements have been carried out at a noise barrier test facility. To study the effect of gaps of different sizes, the sound insulation indices have been measured multiple times with gaps of increasing width opened by wedges between two elements. Specifically, measurements have been carried out for gap widths of 0.1 cm, 0.4 cm, 0.8 cm, 1.5 cm and 2.0 cm. The barrier with the help of which the gaps were studied (figure 3.1) consists of aluminium boxes partly filled with rock wool. The front side of the boxes that would face the noise source in a proper installation are perforated to allow the sound waves to enter the absorbing rock wool. Each acoustic element has a length of 4 m, a height of 50 cm and a thickness of 12 cm. The bottom and top of the elements have a groove and a tongue that fit together, trying to reduce the amount of sound leakage. Hence, the produced gaps don't have a flat shape. For the smaller gap sizes examined it was therefore not possible to look through the gap. Figure 3.6 gives a sketch of the cross section of the produced gaps.

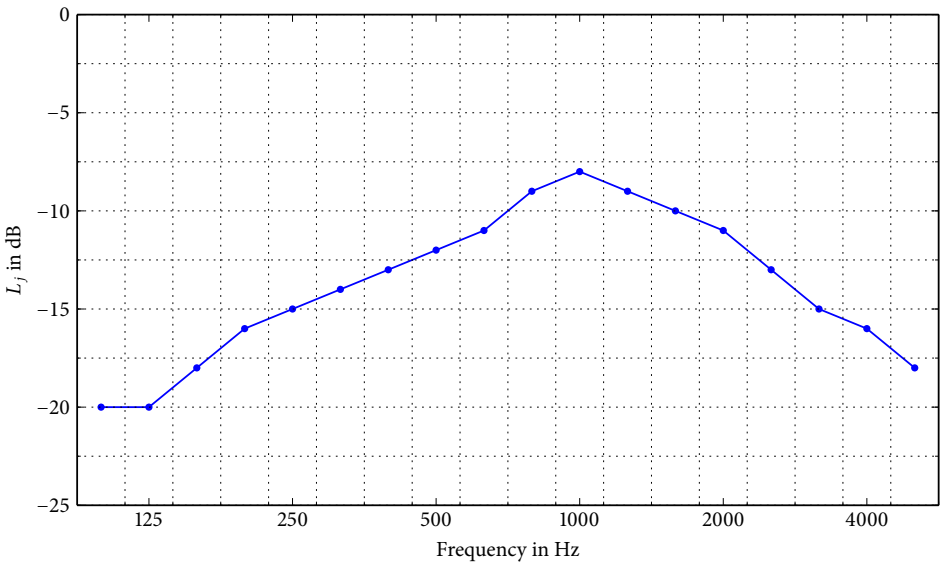

Figure 3.5: Standardised traffic noise spectrum (EN 1793-3)

Frequency	L_j	Frequency	L_j
100 Hz	−20 dB	800 Hz	−9 dB
125 Hz	−20 dB	1000 Hz	−8 dB
160 Hz	−18 dB	1250 Hz	−9 dB
200 Hz	−16 dB	1600 Hz	−10 dB
250 Hz	−15 dB	2000 Hz	−11 dB
315 Hz	−14 dB	2500 Hz	−13 dB
400 Hz	−13 dB	3150 Hz	−15 dB
500 Hz	−12 dB	4000 Hz	−16 dB
630 Hz	−11 dB	5000 Hz	−18 dB

Table 3.1: Standardised traffic noise spectrum (EN 1793-3)

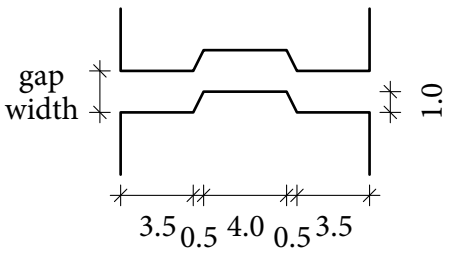

Figure 3.6: Cross section of the gap in the noise barrier where the measurements were carried out. Indicated lengths in cm

Figure 3.2 contains a sketch of the measurement setup: Both the loudspeaker and the gap were positioned at a height of 2.5 m above ground level. For the two conditions without any gap and with a 2 cm gap, a large number of microphone points were evaluated. The results of these measurements showed that for this unstructured barrier the variation of the sound insulation indices between different microphone points at the same height was negligible. In order to be able to examine a larger number of gap widths, the remaining measurements were made for microphone points only in one vertical line. Chapter 5.5 contains a number of figures presenting the variation of the sound insulation for different positions behind the barrier; in particular figure 5.13 shows the variation for 17 different vertical positions for the 2 cm gap. In order to use the same positions for all gap widths, for the third-octave band sound insulation indices presented later on in this thesis only the following five positions have been taken into account: 40 cm above the gap, 20 cm above, directly at the same height as the gap and 20 cm and 40 cm below the gap.

The measurements were carried out using an MLS sequence of 65 535 samples played back at 48 kHz. The MLS sequence was repeated 32 times and the average over the impulse responses calculated. The barrier was 4.5 m high, therefore the Adrienne window did not need to be shortened. Figure 3.3 shows the measured and windowed impulse response of the central microphone position directly behind the gap with a gap width of 0.4 cm. (The components diffracted over the barrier only arrive so late that they are outside of the shown time frame.) A Brüel&Kjær OmniSource loudspeaker type 4295 was used for the playback of the MLS. The microphone employed for the measurements was a MicW i436 omnidirectional condenser microphone that complies to IEC 61672-1 class 2 [30]. For digitising the signal, an RME Fireface UFX was used. This interface has high quality analogue digital converters and the amplification values can be set digitally and therefore reproducibly. Because determining the sound insulation indices only involves the ratio of sound energy between two measurements conducted directly after each other, a calibration of the whole measurement chain was not necessary.

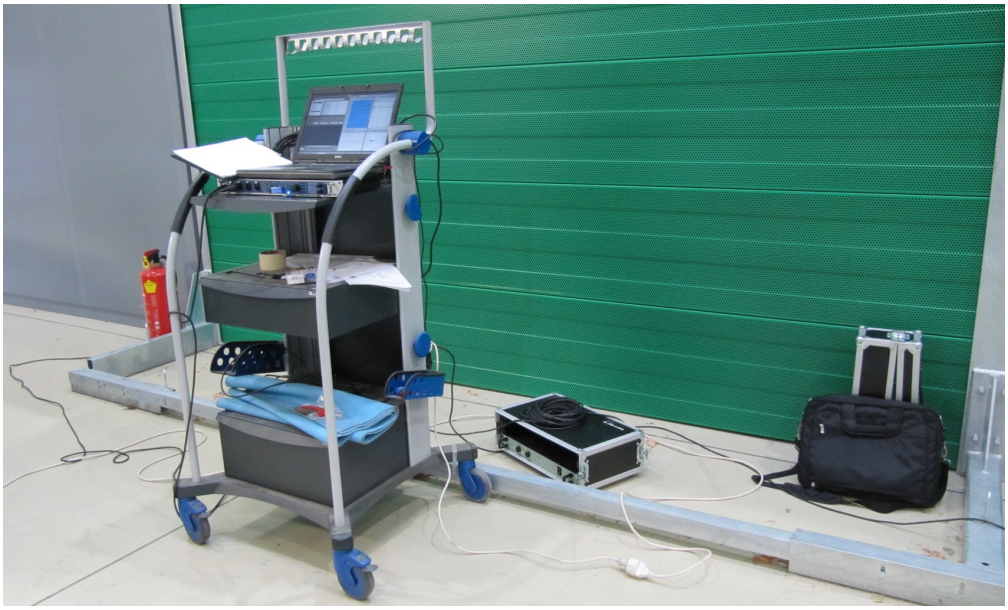

Figure 3.7: The computer, audio interface and amplifier that were used for the measurements

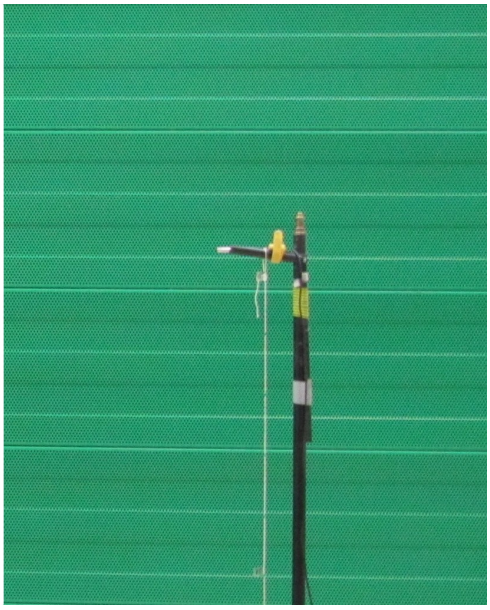

Figure 3.8: The loudspeaker and microphone that were used for the measurements

4 Simulation

4.1 Calculating Impulse Responses with BEM

In order to get results that are comparable to the usual measurements of the sound insulation of noise barriers like the one described in the previous chapter, the simulations were set up in a way that allowed calculating impulse responses.

The boundary element method produces sound pressure values for a given frequency. In contrast to the data obtained by measurement microphones, the simulated sound pressure values are complex, that means in addition to the amplitude they contain phase information. Equation 2.41 says that a conjugate-complex symmetric frequency spectrum corresponds to real sample values in the time domain. To apply this relation, two properties of the FFT have to be taken into account: Firstly, the FFT needs a sample count of 2^N. This requirement can easily be satisfied by zero-padding the spectrum at the end. Adding zeros above the maximum simulated frequency is like specifying that the sound pressure measured at the frequencies above the highest frequency of interest is zero and does not add an error. Secondly, the FFT requires that the frequency values are equally spaced. This goes against the convention to use a logarithmic frequency scale due to the logarithmic human perception of pitch. In other words, the FFT requires that for higher frequency third-octave bands considerably more values need to be calculated than for lower frequency third-octave bands.

This is especially unfortunate, as calculating a result with a given accuracy for a higher frequency requires substantially more computing power than for a lower frequency. The computationally most demanding part in the boundary element method lies in solving the linear system of equations given in equation 2.63. The time necessary to solve a linear system of equations of order N is proportional to N^3. In the case of the BEM, the order N equals the number of panels on the surface. The accuracy of a BEM simulation is determined by the density of the mesh, usually specified as the number of panels per wavelength. Doubling the frequency for a simulation in three dimensions means that the number of panels in a given area quadruples if the result should be of comparable accuracy. That means that the required computing time for one single frequency is proportional to the frequency to the power of six. The total calculation time for a range of frequencies as a function of the maximum frequency is the integral over the time it takes to calculate

the sound pressure for a single frequency and therefore proportional to the frequency to the power of seven. In other words, doubling the maximum frequency means that the calculation of the full frequency range will take about 128 times as long.

Say, the complex sound pressure values $p(f)$ have been calculated for the frequency range up to 5000 Hz with a frequency spacing of 2 Hz. The real impulse response can now be calculated by applying the discrete FOURIER transform to the following array:

$$\begin{bmatrix} 0 \\ p[2\,\mathrm{Hz}] \\ p[4\,\mathrm{Hz}] \\ \dots \\ p[4998\,\mathrm{Hz}] \\ p[5000\,\mathrm{Hz}] \\ 0 \\ \dots \\ 0 \\ p^*[5000\,\mathrm{Hz}] \\ \dots \\ p^*[2\,\mathrm{Hz}] \end{bmatrix} \tag{4.1}$$

There should be 3191 zeros between $p[5000\,\mathrm{Hz}]$ and $p^*[5000\,\mathrm{Hz}]$ so that the total length of the array becomes suitable for the FFT: 2501 + 3191 + 2500 = 8192 = 2^{13}.

Results from computer simulations are exactly reproducible and don't contain errors due to small differences in the positioning of the microphones for instance. Therefore it is possible to create two simulations for very similar conditions and calculate the differences between the two impulse responses. This fact was put to use for this thesis: For every simulated noise barrier with a gap or a hole, a noise barrier without any gap but otherwise identical in its size was simulated and the difference between the two impulse responses for every microphone position was calculated in order to try to remove the components diffracted over the top of the barrier.

Two independent pieces of software were used for the BEM simulations, one operating in three dimensions and one in two.

4.2 Acousto (3D BEM software)

Acousto [18], short for Acoustic Simulation Tool, is an open source boundary element solver written by Umberto Iemma and Vincenzo Marchese of the Roma Tre University. It is written in the programming language C and uses the OpenMPI [20] library to distribute

the computation over multiple processors or multiple computers. For this thesis, Acousto version 1.5 was used.

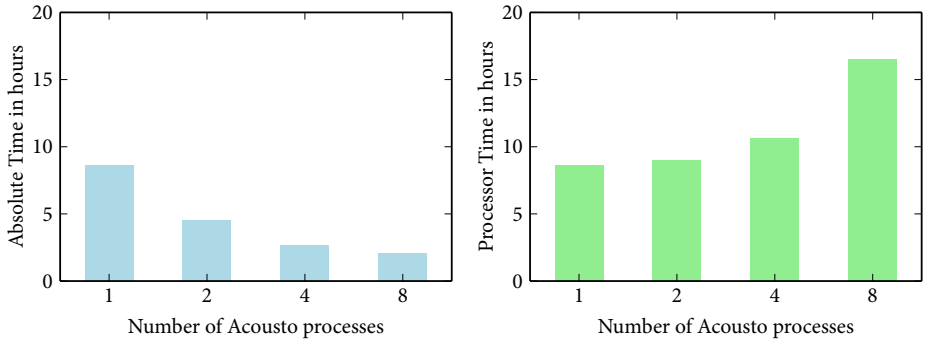

Figure 4.1: Time it took to calculate a given problem size with Acousto. Blue is the absolute time from start to finish ("wall clock time"), green is the absolute time multiplied with the number of Acousto processes ("used processor time")

The option to distribute the computing load over multiple processors sounds promising, but is only of limited use in practice. The problem is that solving a large system of linear equations with a dense coefficient matrix is a task that is not easy to parallelise. Figure 4.1 gives an example of the used calculation times for a given problem size using one, two, four or eight Acousto processes (BEM matrix of the order $N \approx 11500$, 20 frequencies around 3600 Hz calculated, 25 GB of RAM used). One can see that distributing the load onto multiple processors is not very efficient regarding the total processor time used. For this thesis another approach was taken: Instead of running only one Acousto job distributed over a larger number of processes at a time, multiple Acousto jobs for different frequencies were started in parallel. By doing so, all processors in the calculation server could be used in a more efficient way. Unfortunately, this approach has another drawback:

Acousto starts by calculating the integral coefficients representing the influence of each panel onto the collocation points on each panel and onto the microphone points. From these coefficients, the matrix describing the linear system of equations (H in equation 2.63) can be calculated. Unfortunately, these coefficients need a lot of memory; for the 5000 Hz calculation for the problem size used in this thesis the amount of storage occupied during the calculation was over 60 GB. Acousto allows to choose whether it should store this huge amount of data in memory or write it to disk, but both options have their drawbacks: The calculation server that most of these calculations have been performed on has 48 GB of RAM and two processors with six cores each, making it only 4 GB per processor core – far too little to store all coefficients in RAM only. Writing to and reading from the hard disk is not so much a problem for one single Acousto process, because most access is sequential anyway – just the kind of access that spinning hard drives deliver the best speed

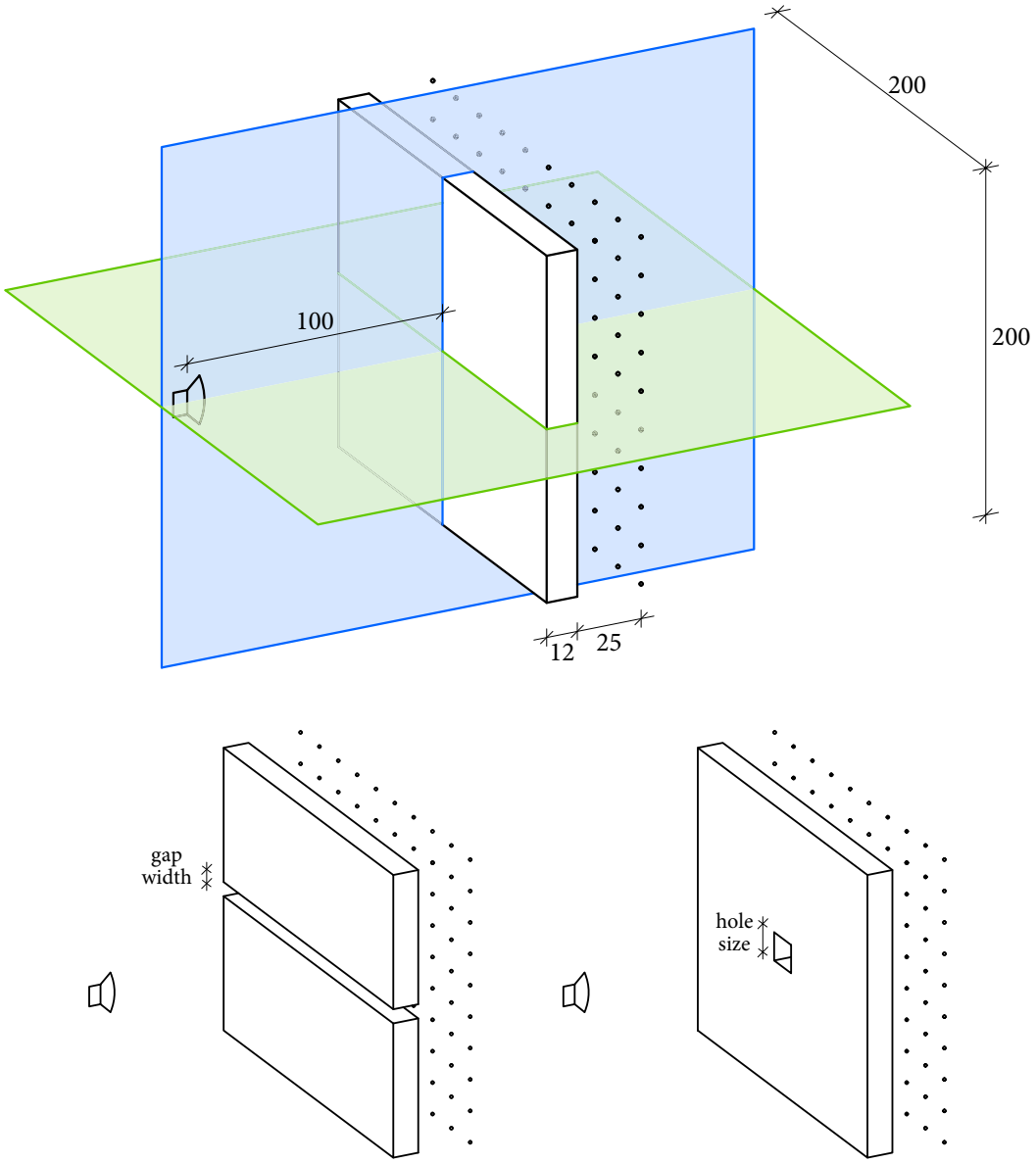

Figure 4.2: Sketches of the 3D simulations: Top: Loudspeaker on the left hand side. Noise barrier with any gap in the middle. Dots on the right hand side indicate the microphone positions where the sound pressure was calculated. (Not all microphones shown.) Symmetry planes are plotted blue and green. Indicated lengths in cm. Bottom left: Noise barrier with a gap. Bottom right: Noise barrier with a hole

at. Running multiple separate Acousto jobs in parallel however results in rapid jumping back and forth of the heads of the disk at times and therefore a dramatically declining total read rate, again increasing the time an Acousto job takes because the processor needs to wait for its data. Overall, the following middle ground has been used for this thesis: The LAPACK installed on the computing server, ATLAS [21], always used two threads, meaning that for every Acousto process two processor cores were put to use. Figure 4.1 shows that the trade-off for two Acousto processes is not as big as for higher numbers of parallel processes. Therefore, each Acousto job was configured to use two Acousto processes and thus utilise four processor cores. With twelve processor cores available in the computing server, three Acousto jobs were started concurrently. Each Acousto job utilising four cores was also a good fit for two desktop computers with quad-core processors that were available for calculations during the holidays.

Acousto allows to specify symmetry planes. Symmetries in the BEM are accounted for by changing the Green's function and consequently every symmetry plane cuts the order of the system of equations in half, thereby reducing the time to solve the system to one eighth. To deal with the non-uniqueness problem, Acousto implements the CHIEF method. Unfortunately, a lot of CHIEF points are needed to successfully remove all fictitious resonances, thereby significantly increasing the computation time.

For the final calculations, a Python [23, 24] script was developed that started with the maximum frequency 5000 Hz, took the next 10 frequencies (say, 4982, 4984, 4986, …, 5000 Hz for a frequency spacing of 2 Hz), generated a mesh suitable for the highest frequency in the current range, generated the necessary Acousto configuration files, copied these files to the calculation server and started Acousto there. Then these steps were repeated two more times for the calculation server and for each of the desktop workstations until each computer participating in the calculations was busy with calculations. Once an Acousto job finished, the Python program fetched the results and created a new job for the computer until the whole frequency range 0 Hz to 5000 Hz was processed. By using this approach, the available computing resources were used as efficiently as possible.

4.3 OpenBEM (2D BEM software)

OpenBEM [19] is a collection of Matlab [22] programs for solving the Helmholtz equation developed by Peter Juhl and Vicente Cutanda Henríquez of the University of Southern Denmark. OpenBEM allows the treatment of problems in three dimensions generally, with axisymmetry or in two dimensions. For this thesis, OpenBEM was used for BEM simulations in two dimensions.

In two dimensional BEM simulations there are no point sources; instead all sources are line sources. To account for this change of the propagation characteristics, a different Green's function needs to be used and the Helmholtz radiation condition changes slightly.

OpenBEM does not really have a user interface. Instead, the user directly faces the program code that sets up the relevant matrices and solves the system of equations. For this study, the sample code given for noise barriers was put into a Matlab class with functions for creating rectangular reflecting surfaces, setting the position of the line source, setting up the microphone positions, calculating the pressure values on the surface and finally calculating the pressure values at the microphone positions. This class loses some of the options of the original code like creating irregularly shaped or even bended surfaces or changing the position of the CHIEF points, but was more convenient for automatically adjusting the sizes of the gaps or the position of the source. Additionally, some parts of OpenBEM were slightly changed to use multiple processors – Matlab offers a very convenient way to parallelise loops by replacing the command "for" with "parfor" and telling Matlab which variables are local to one iteration of the loop and which are global for the whole program. Finally, a Matlab script was written that again loops over all frequencies.

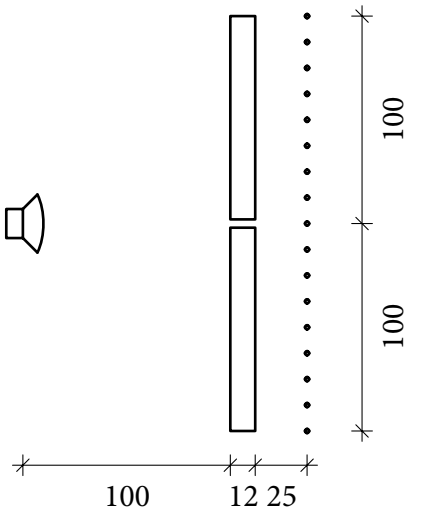

Figure 4.3: Sketch of the 2D simulation: Loudspeaker on the left hand side. Noise barrier with a gap in the middle. Dots on the right hand side indicate the microphone positions where the sound pressure was calculated. (Not all microphones shown.) Indicated lengths in cm

4.4 Simulated Noise Barrier

To get the problem down to a reasonable computation time, the size of the simulated barrier was rather small. The standard EN 1793-6 expects the wall to have a height of at least 4 m so that sound diffracted over the top arrives only after the end of the Adrienne window and is therefore not evaluated. For the simulations however, the height of the noise barrier was reduced to only 2 m. Accordingly, the Adrienne windows were shortened and the low frequency limit increased. All of these adjustments were done for each microphone position individually so that microphones higher up that would be reached by sound diffracted over the top earlier had a shorter Adrienne window than those microphones further down.

Additionally, for the 3D simulations two symmetry planes were introduced: One plane cuts through the middle of the simulated gap in the barrier and the other plane is orthogonal to both the first symmetry plane and the barrier. The disadvantage of this approach is that the gap itself needs to be symmetric and therefore cannot include a groove and a tongue like the barrier at which the measurements have been carried out.

The other properties were chosen similar to the measured barrier: The thickness of the barrier was 12 cm, the surfaces fully reflective, the source centred 1 m in front of the barrier and the microphones 25 cm behind the barrier. Figures 4.2 and 4.3 give sketches of the setup.

For the 2D simulations the CHIEF technique was employed as a measure against the non-uniqueness problem, but for the 3D simulations CHIEF was not used in order not to increase the calculation time even further. Figure 4.4 gives an example of the output of a simulation for the microphone position centred directly behind the gap: The plotted values are "single-frequency sound insulation indices", that means for every frequency the energy in the simulation with the barrier was compared to the energy in the free-field simulation. The data displayed in figure 4.4 is nearly the direct output of the simulations without the Adrienne window applied; it is therefore not comparable to the third-octave band sound insulation indices presented later on. Figure 4.4 shows the effect of the non-uniqueness problem: The red curve represents the 2D simulation, which was carried out with CHIEF points and is rather smooth, whereas the blue curve, which represents the comparable 3D simulation without the CHIEF technique, is only smooth for lower frequencies and contains lots of spikes above a frequency of about 1400 Hz. The limit frequency of 1400 Hz, above which the fictitious resonances can be observed, corresponds to a wavelength of about 24 cm, which is double the thickness of the barrier.

In order to decide which frequency spacing to use, the first 3D simulations were run with a frequency spacing of 1 Hz. Using the computing server and two desktop computers, the first simulation took approximately ten days. Evaluating the results for all 5000 frequencies

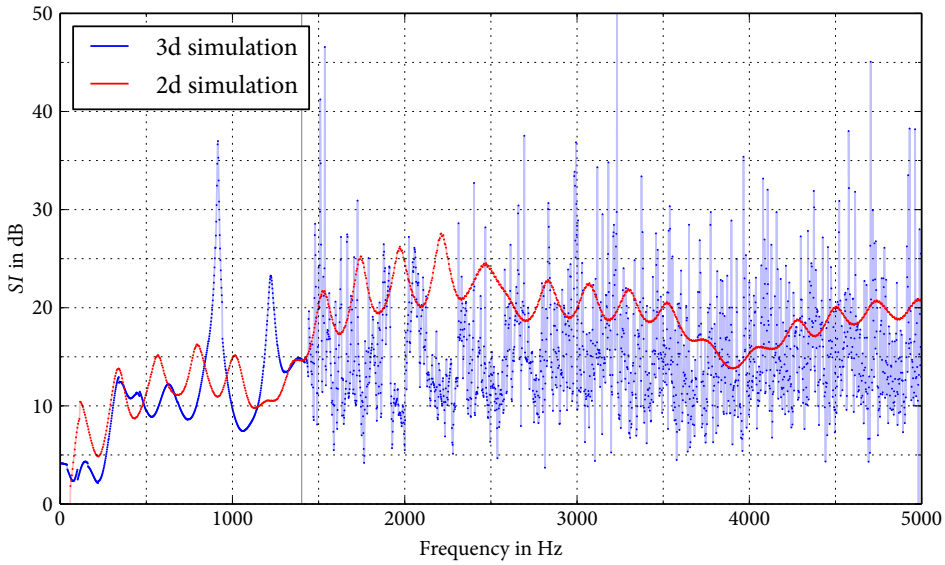

Figure 4.4: Unwindowed output of the simulation for a single microphone position. The spikes in the blue curve above 1400 Hz are the result of the non-uniqueness problem (CHIEF was only used for the 2D simulations)

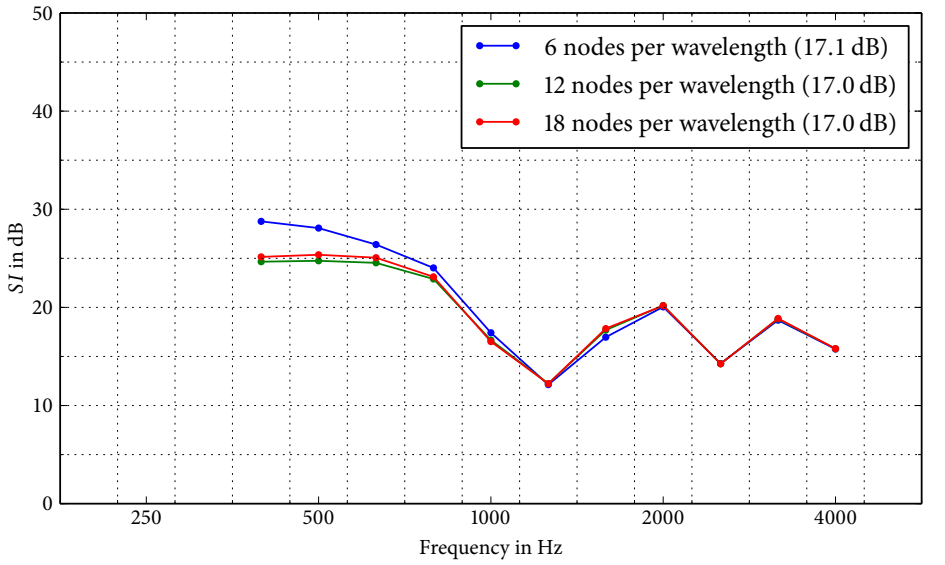

Figure 4.5: Sound insulation of noise barriers with gaps (2D simulation). Compare different densities of the applied BEM mesh

and comparing with subsets with higher frequency spacing only showed changes if the frequency spacing was significantly increased. Therefore, all following 3D simulations were performed with a doubled frequency spacing of 2 Hz. Because the results obtained from 2D simulations were smoother due to the use of the CHIEF technique, a frequency spacing of 4 Hz was used for the 2D simulations.

The last remaining question concerns the appropriate mesh density. In order to get an acceptable balance between reliability of the results and calculation times, the same 2D simulation has been carried out multiple times with mesh densities of 6, 12 and 18 nodes per wavelength. The calculation times for these three simulations were about 12, 41 and 88 hours. Figure 4.5 gives the result of this comparison. It seems that the error for the smallest mesh density of 6 nodes per wavelength is rather small for most third-octave bands; therefore all meshes used for this thesis were generated with 6 nodes per wavelength.

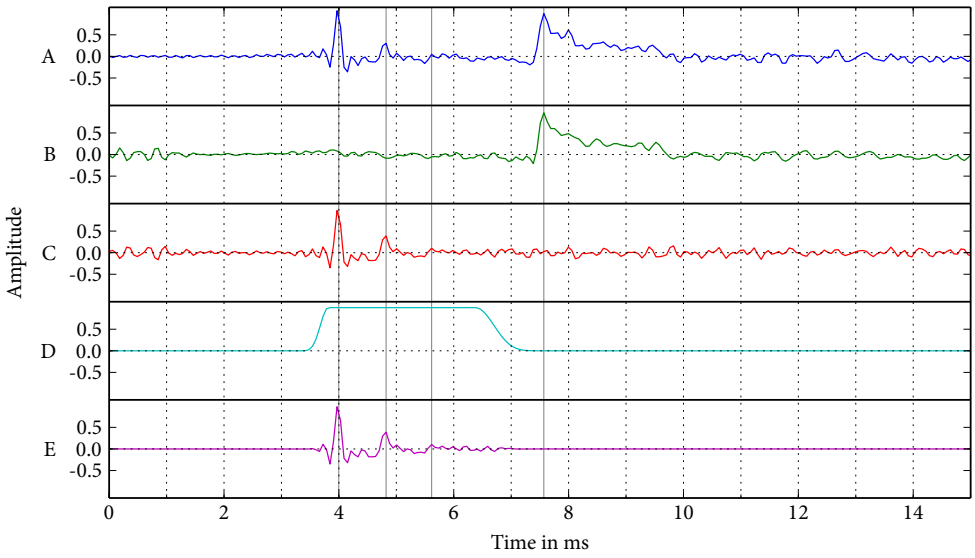

Figure 4.6: Simulated impulse responses in 3D of the microphone at the centre position. A: Barrier with a 1 cm gap. B: Barrier without a gap. C: A minus B. D: Adrienne window. E: Windowed impulse response

Figures 4.6 and 4.7 give two examples for the processing of the impulse responses. The first of the five graphs (A) displays the impulse response directly obtained from the FOURIER transform of the sound pressure values produced by Acousto and OpenBEM. The second graph (B) shows the impulse response of the same barriers, but without any gap; that means that everything seen in B should come from components diffracted around the barrier. Graph C shows the difference between A and B: The peak from the components

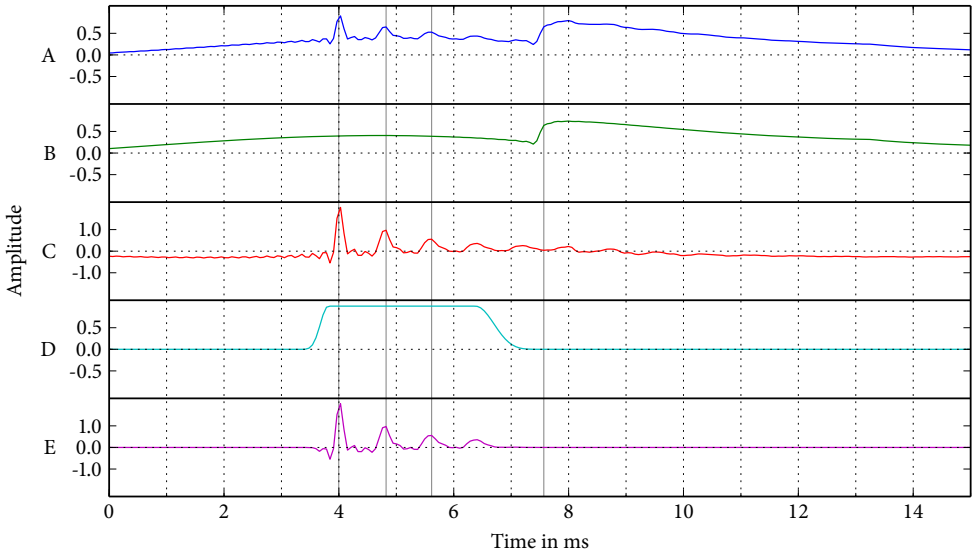

Figure 4.7: Simulated impulse responses in 2D of the microphone at the centre position. A-E like in figure 4.6

diffracted around the barrier vanishes and almost only the peaks from the components transmitted through the gap remain. The fourth graph (D) shows the Adrienne window and the fifth graph (E) is the window D applied to the impulse response C. The impulse response shown in this last graph was used for the evaluation of the sound insulation index.

The limits of the simulation method can be seen in the calculated impulse responses. The 2D simulations show a nearly-constant shift in the simulated impulse responses A and B. Both impulse responses are not zero before the arrival of the expected peaks. For the higher mesh density simulations mentioned before, this slowly changing component that physically should not be there is considerably smaller. Fortunately this shift is nearly the same for both the simulation with a gap (graph A in figure 4.7) and the one without any gap (graph B); therefore the nearly-constant shift can be mostly cancelled out simply by calculating the difference between the two simulated impulse responses (graph C).

The impulse responses obtained from 3D simulations don't have a nearly-constant shift like the 2D ones, but they exhibit small fluctuations that look like noise. They are mostly the result of the non-uniqueness problem – impulse responses calculated only from the frequencies 0-1400 Hz are much smoother.

Both 2D and 3D simulations show very well that multiple reflections at the front and rear end of the gap occur. The first peak occurs at approximately 4 ms, which corresponds to a

sound path of 4×10^{-3} s $\cdot$ 343 m/s = 1.37 m and is what one would expect from geometric considerations (see figure 4.3). The next two peaks follow at approximately 4.8 ms and 5.6 ms, with an interval corresponding to a sound path of 0.8×10^{-3} s $\cdot$ 343 m/s $\approx$ 0.27 m. Double the barrier thickness is 0.24 m, hence one can follow that the imaginary reflection point is not in the plane of the front or back side of the barrier, but a little beyond. Comparison of the intervals between the peaks between simulations with different gap widths shows that for higher gap widths the intervals increase marginally, putting the imaginary reflection point a little further away from the barrier.

5 Results and Discussion

5.1 Measurement

Measurements have been carried out at a noise barrier of a thickness of 12 cm made from aluminium boxes partly filled with rock wool. Figure 5.1 shows the sound insulation indices SI in third-octave bands for the barrier without any gap and for the same barrier with gaps of different sizes. The single-number ratings DL_{SI} are given in table 5.1.

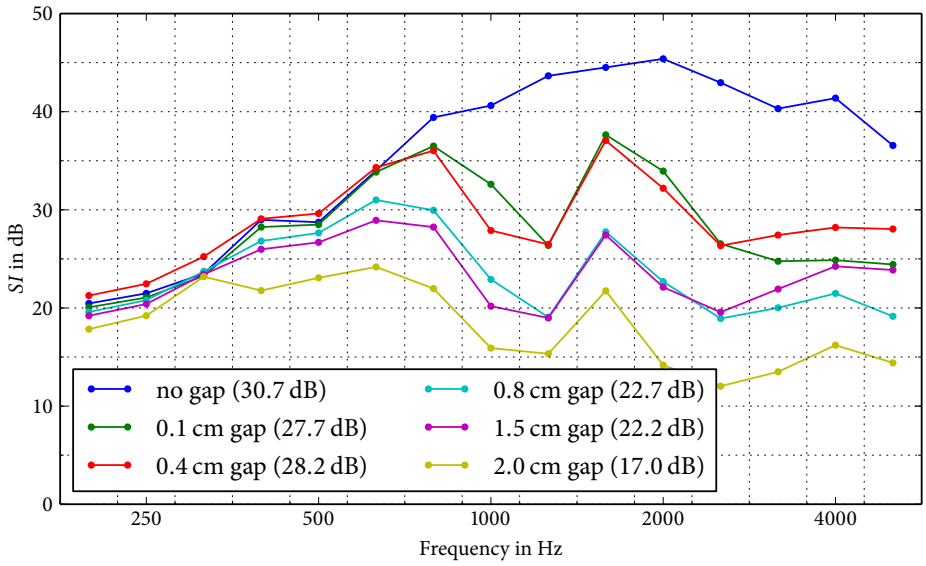

Figure 5.1: Measured sound insulation of noise barriers with gaps. Numbers in brackets in the legend are the single-number ratings $DL_{SI}^{200-5000\,\mathrm{Hz}}$

The sound insulation indices SI of the intact barrier start at about 20 dB at the lowest frequency band at 200 Hz, then increase for higher frequencies to 40 dB at the 800 Hz band and stay above 40 dB for nearly all of the remaining frequency bands. The SI measured with a gap in the barrier have a very different shape: There is a significant impact especially in the higher frequency bands; in particular for nearly all frequency

gap width	measurement	
	$DL_{SI}^{200-5000\,\mathrm{Hz}}$	$DL_{SI}^{400-4000\,\mathrm{Hz}}$
no gap	30.7 dB	35.9 dB
0.1 cm	27.7 dB	29.7 dB
0.4 cm	28.2 dB	29.4 dB
0.8 cm	22.7 dB	22.9 dB
1.5 cm	22.2 dB	22.3 dB
2.0 cm	17.0 dB	16.8 dB

Table 5.1: Measured sound insulation: Single-number ratings DL_{SI} for gaps. The single-number rating $DL_{SI}^{200-5000\,\mathrm{Hz}}$ covers the largest reliable frequency range; for better comparability with the simulations the single-number rating $DL_{SI}^{400-4000\,\mathrm{Hz}}$ covering only a reduced frequency range is also given

bands above 1000 Hz the sound insulation index is reduced by more than 10 dB. Relative minima can be observed in the graphs for all gaps at the 1250 Hz and the 2500 Hz bands. The single-number ratings DL_{SI} are also significantly impacted by the gaps.

Comparing the *SI* of the different gap widths with each other shows an unexpected property: There are two pairs of gap widths with overlapping curves. For both the 0.1 cm and 0.4 cm gap pair and the 0.8 cm and 1.5 cm gap pair the DL_{SI} are very similar. In most frequency bands the two *SI* of each pair are fairly close to each other; there are only a few frequency bands where the *SI* of one curve of each pair is higher and a few other frequency bands where the *SI* of the same curve is lower than the *SI* of the other curve of the pair. In his study of the effect of apertures on the sound insulation of walls, Gomperts [14] found a region of gap widths in which the sound insulation at the resonance frequencies is nearly independent of the gap width. The gaps that the measurements have been performed on have a very different, more complicated cross section than those analysed by Gomperts, so his conclusion cannot be directly applied here, but at least Gomperts's findings show that certain physical effects can lead to unexpected variations of the sound insulation. Further investigations need to be done to find out the reason for the observed grouping of gap widths.

Finally, the author wants to stress again what he regards as a significant result: Even though the 0.1 cm gap was not really possible to spot without using a ruler, there is already a significant impact in the sound insulation. The single-number rating $DL_{SI}^{200-5000\,\mathrm{Hz}}$ decreases about 3 dB, but even more important is that the sound insulation indices *SI* in most frequency bands above 1000 Hz are reduced by more than 10 dB!

5.2 Simulation

Three different series of simulations have been carried out. In the first series the **impact of the size of the gap** on the sound insulation has been analysed. Simulations have been carried out in both 2D and 3D for gaps of four different sizes between 0.5 cm and 5 cm in a barrier of the same thickness as the barrier where the measurements have been performed (12 cm). The sound insulation indices *SI* in third-octave bands calculated from these simulations can be seen in figures 5.2 (2D) and 5.3 (3D) and the corresponding single-number ratings $DL_{SI}^{400-4000\,\mathrm{Hz}}$ are listed in table 5.2.

gap width	2D simulation	3D simulation
0.5 cm	21.1 dB	22.3 dB
1 cm	17.1 dB	18.8 dB
2 cm	13.9 dB	16.3 dB
5 cm	10.3 dB	11.3 dB

Table 5.2: Simulated sound insulation: Single-number ratings $DL_{SI}^{400-4000\,\mathrm{Hz}}$ for gaps in a 12 cm barrier

For all simulated gaps in 12 cm barriers there are at least two obvious relative minima, one approximately in the 1250 Hz band and one in the 2500 Hz band. The presentation in third-octave bands makes it impossible to determine the exact frequencies of the minima, but the results in figure 5.2 (2D) suggest that with increasing gap sizes the minima move slightly to lower frequencies: For the 0.5 cm gap the first minimum is in the 1250 Hz frequency band and of the adjacent frequency bands the sound insulation index of the 1600 Hz band is significantly lower than the one of the 1000 Hz band, suggesting that the minimum is rather in the upper part of the 1250 Hz band. Looking at the 1 cm gap, the first minimum again is in the 1250 Hz band, but this time the *SI* in the two neighbouring frequency bands is approximately equal. Continuing with the 2 cm gap, the first minimum still is in the 1250 Hz band, but the adjacent sound insulation indices suggest that the real minimum frequency is rather in the lower part of the 1250 Hz band. Finally, with the largest gap, the 5 cm gap, the first minimum sits unambiguously in the 1000 Hz band and accordingly continues the movement to lower frequencies with increasing gap width. The 3D simulations (figure 5.3) show a similar tendency: The first minimum of the 0.5 cm gap clearly is in a higher frequency band than the first minimum of the 5 cm gap.

Comparing the minima in the 2D simulations to those in the 3D simulations shows that the frequencies of the minima are rather similar, but for the 3D simulations the minima seem to be at slightly lower frequencies. A minor discrepancy between the 2D and 3D results is to be expected because of the different simulated setting: The 3D simulation

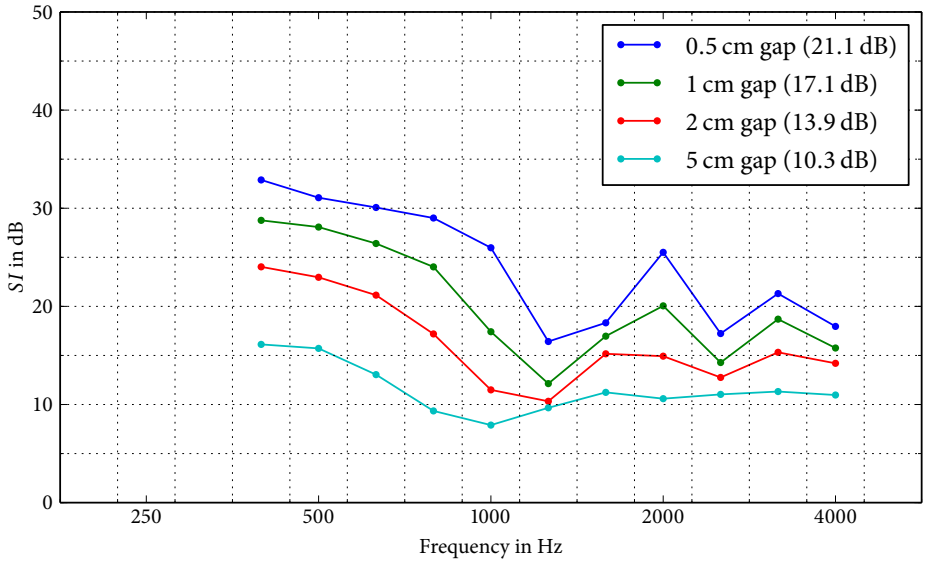

Figure 5.2: Sound insulation of noise barriers with gaps from 2D simulations. Numbers in brackets in the legend are the single-number ratings $DL_{SI}^{400-4000\,\mathrm{Hz}}$

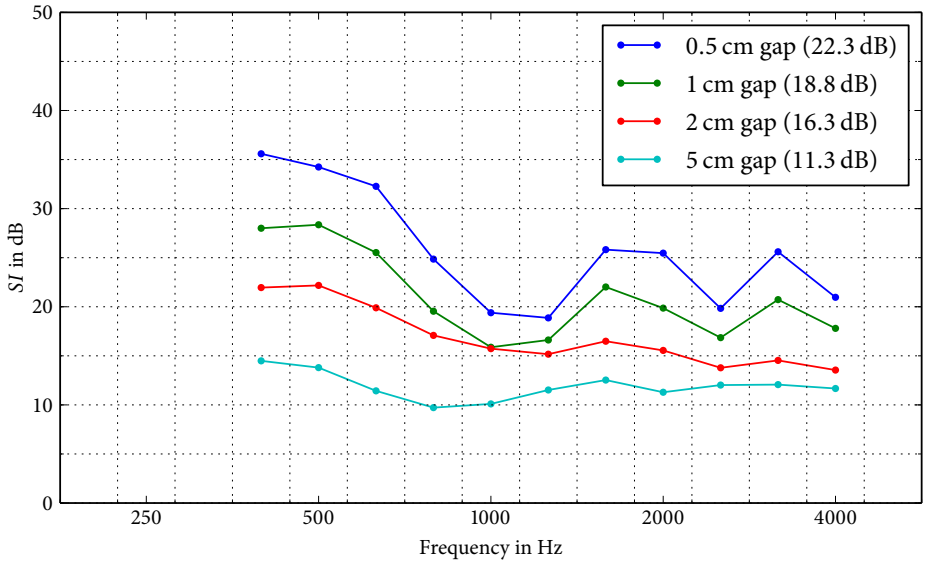

Figure 5.3: Sound insulation of noise barriers with gaps from 3D simulations. Numbers in brackets in the legend are the single-number ratings $DL_{SI}^{400-4000\,\mathrm{Hz}}$

assumes a point source and spherical waves, whereas the 2D simulation uses a line source and cylindrical propagation characteristics.

Considering the general change of the magnitude of the *SI* and the depth of the minima, one can see that generally smaller gaps lead to higher sound insulation as expected. This is true for the single-number ratings $DL_{SI}^{400-4000\,\mathrm{Hz}}$ and also for the sound insulation indices *SI* in nearly all frequency bands, but at the frequency bands of the minima the difference in the *SI* is smaller than at frequency bands far from the minima. In other words, for smaller gaps the depth of the minima is larger, but not large enough to compensate the generally better sound insulation of smaller gaps.

The second series covers the **impact of the barrier thickness** and comprises 3D simulations of 1 cm gaps in barriers of a thickness of 8 cm, 12 cm and 16 cm. The resulting sound insulation indices *SI* are given in figure 5.4 and the single-number ratings $DL_{SI}^{400-4000\,\mathrm{Hz}}$ are listed in table 5.3.

barrier thickness	3D simulation
8 cm	19.8 dB
12 cm	18.8 dB
16 cm	18.7 dB

Table 5.3: Simulated sound insulation: Single-number ratings $DL_{SI}^{400-4000\,\mathrm{Hz}}$ for 1 cm gaps in barriers of different thicknesses

The relative minima of the *SI* in this second series of simulations occur at very different frequency bands for barriers of different thicknesses. The shapes of the curves are rather similar though; the changes look akin to simple shifts of the whole curve to higher frequencies for the thinner barriers. The depths of the minima seem to be nearly the same and the general magnitudes of the *SI* are also very close to each other. The $DL_{SI}^{400-4000\,\mathrm{Hz}}$ differ a bit, but that is to be expected because of the weighting with the traffic noise spectrum. Comparing the shift of the minima observed here with the one observed in the first series of simulations shows that the barrier thickness has a larger impact on the position of the minima than the width of the gap: Doubling the barrier thickness moves the frequency of the first minimum of the *SI* further than even a tenfold increase of the gap width. The overall sound insulation described by the $DL_{SI}^{400-4000\,\mathrm{Hz}}$ though depends more on the size of the gap than the thickness of the barrier.

Finally, in the third series of simulations **quadratic holes** were cut out from barriers of a thickness of 12 cm. Figure 5.5 gives the sound insulation indices *SI* and table 5.4 show the corresponding single-number ratings $DL_{SI}^{400-4000\,\mathrm{Hz}}$.

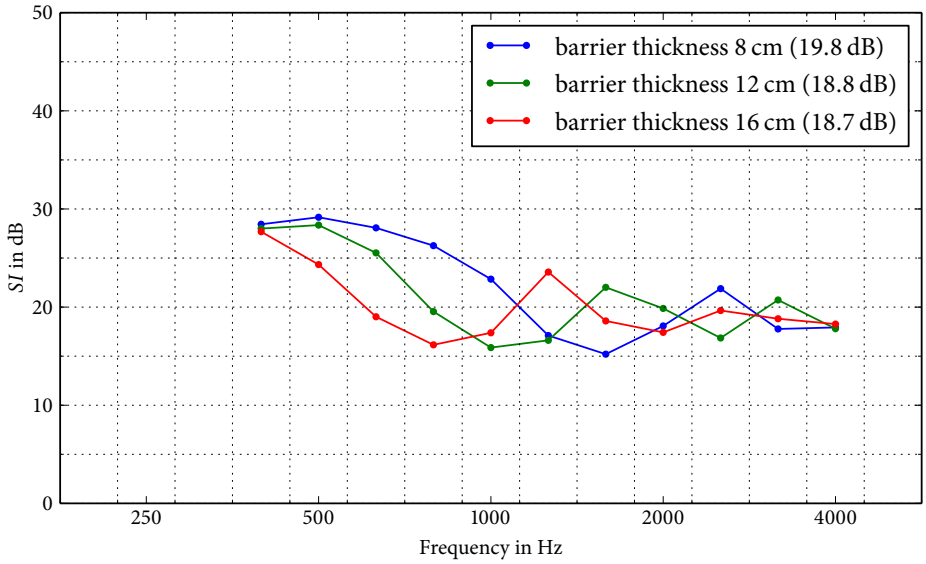

Figure 5.4: Sound insulation of noise barriers of different thicknesses with 1 cm gaps from 3D simulations. Numbers in brackets in the legend are the single-number ratings $DL_{SI}^{400-4000\,\mathrm{Hz}}$

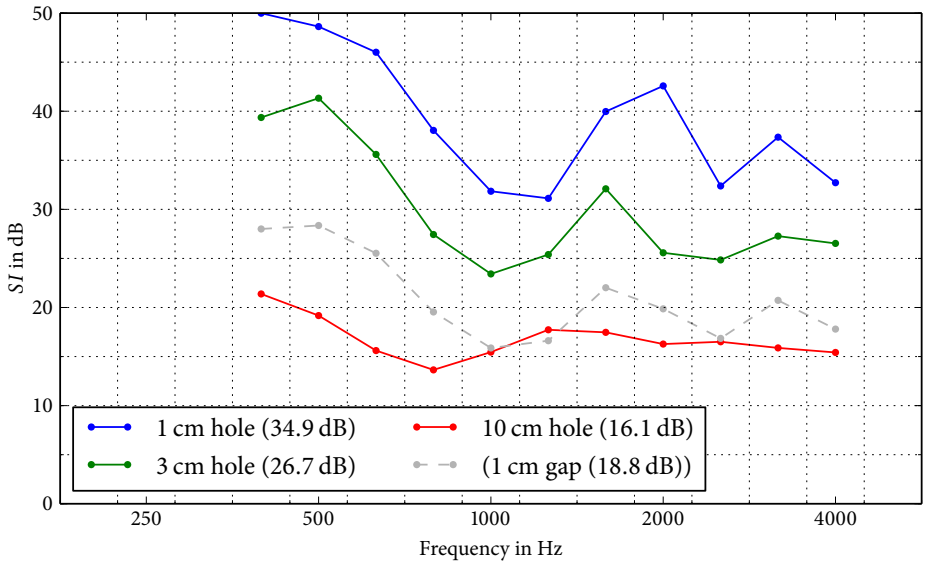

Figure 5.5: Sound insulation of noise barriers with holes from 3D simulations. 1 cm gap shown for comparison. Numbers in brackets in the legend are the single-number ratings $DL_{SI}^{400-4000\,\mathrm{Hz}}$

Again, relative minima of the *SI* can be observed: For the 1 cm × 1 cm hole there are minima in the 1250 Hz band and the 2500 Hz band, and for larger holes these minima move to lower frequencies. The general magnitudes of the sound insulation of the simulated holes are higher than those of the simulated gaps: Even a rather large hole of 3 cm × 3 cm has significantly less impact on the sound insulation of a barrier than a gap of 1 cm. It takes an enormous hole of 10 cm × 10 cm in a barrier for the sound insulation to become worse than the one of a barrier with a gap of 1 cm. One can follow that for barriers where the post needs to be mounted on top of the base of the barrier, a design similar to the one photographed for figure 1.4 is superior to the one depicted in figure 1.3.

hole size	3D simulation
1 cm	34.9 dB
3 cm	26.7 dB
10 cm	16.1 dB

Table 5.4: Simulated sound insulation: Single-number ratings $DL_{SI}^{400-4000\,\mathrm{Hz}}$ for holes in barriers of a thickness of 12 cm

5.3 Analytical formula by Gomperts

The sound insulation index *SI* defined in EN 1793-6 [27] always compares the energies in frequency bands. Gomperts's analytical model lead to the the transmission factor q_{sl}, which compares the energies for individual frequencies though. Despite this different starting point, a comparable curve can still be obtained by calculating the logarithm $-10\log_{10}(q_{sl})$.

Figures 5.6 and 5.7 show the results of Gomperts's formula with the variation of two parameters of the barrier: In figure 5.6 the size of the gap is varied between 0.5 cm and 2 cm and the thickness of the barrier is always 12 cm like in the first series of simulations discussed in chapter 5.2. In figure 5.7 the size of the gap is always kept at 1 cm and the thickness of the barrier is varied between 8 cm and 16 cm like in the second series of simulations. One can see that with different gap widths the frequencies of the minima change only slightly, whereas the thickness of the barrier has a large influence on the frequencies of the minima. The depth of the minima though mostly depends on the gap width and not so much on the thickness of the barrier.

Figures 5.8 and 5.9 show the results from the same calculations, but this time the average for every frequency band has been calculated. The presentation in frequency bands hides some of the information though: Both the frequency and the depth of the minima can

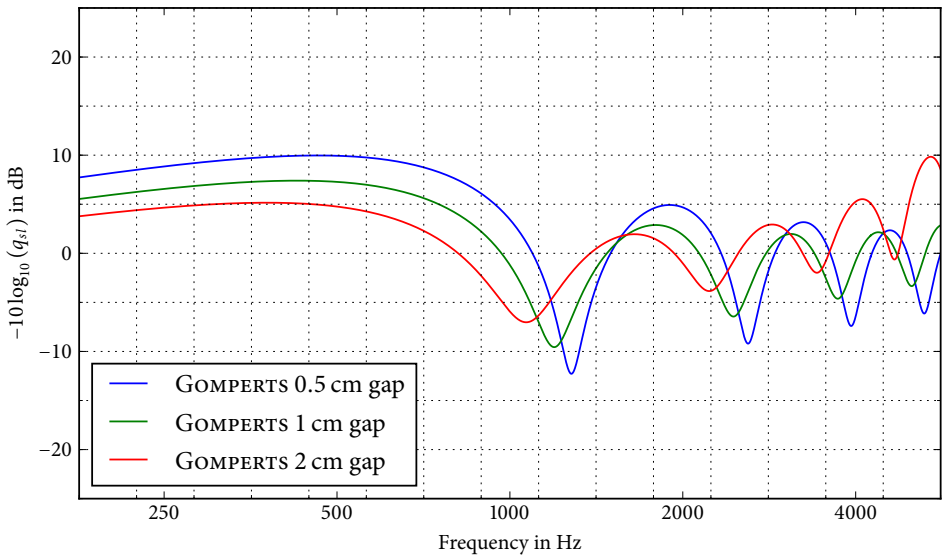

Figure 5.6: Transmission factor as calculated by Gomperts for gaps of different widths in a 12 cm barrier

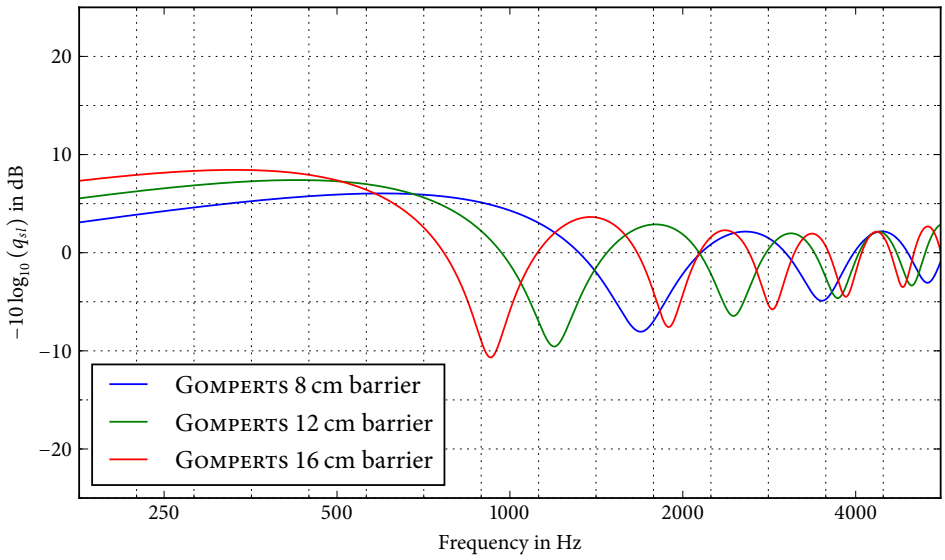

Figure 5.7: Transmission factor as calculated by Gomperts for 1 cm gaps in barriers of different thicknesses

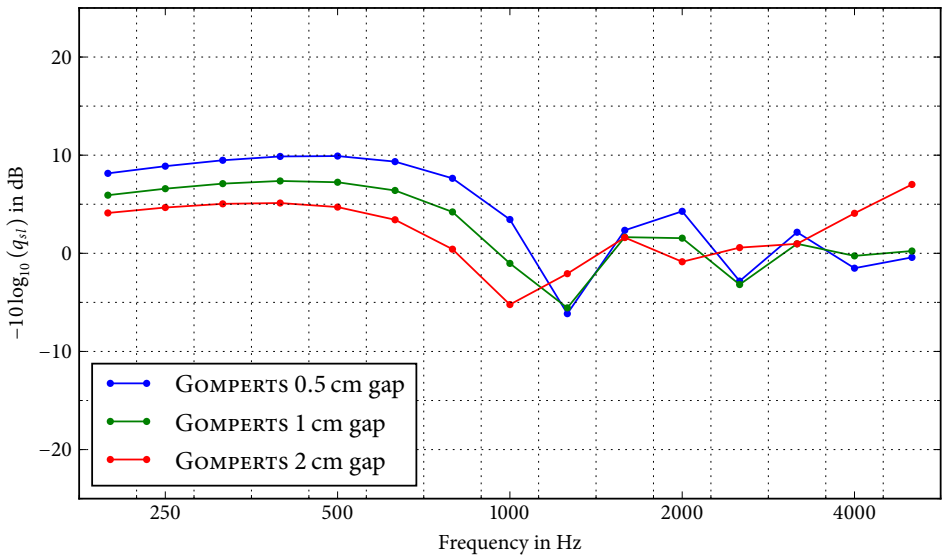

Figure 5.8: Transmission factor as calculated by Gomperts but presented in third octave bands for gaps of different widths in a 12 cm barrier

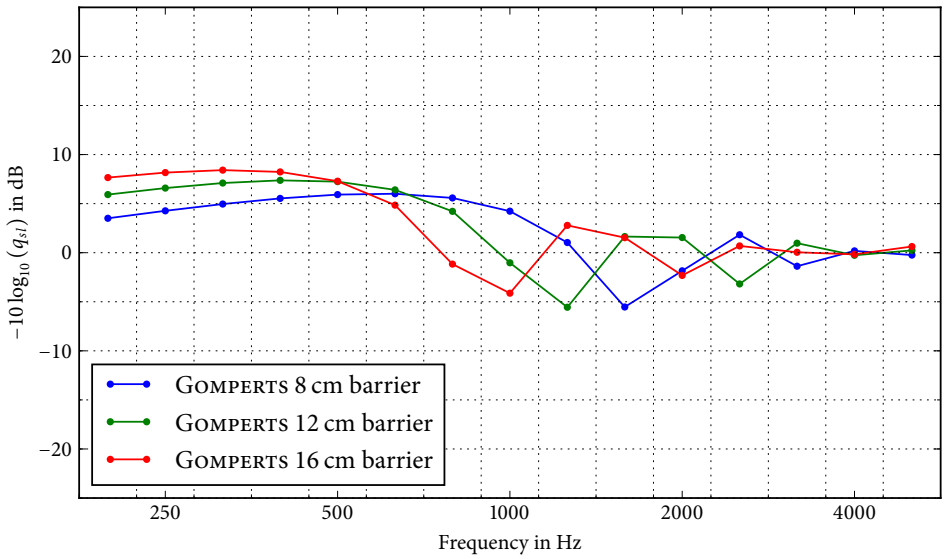

Figure 5.9: Transmission factor as calculated by Gomperts but presented in third octave bands for 1 cm gaps in barriers of different thicknesses

only be determined with less accuracy. To give an example, it is harder to read from figure 5.8 than from figure 5.6 that the first minimum for the 0.5 cm gap (blue) is at a higher frequency than the first minimum for the 1 cm gap (green).

5.4 Comparison and Discussion

All three methods (measurements, BEM simulations, Gomperts's analytical formula) show minima in the sound insulation at roughly the same frequencies for barriers of a thickness of 12 cm. No measurements have been performed for barriers of other thicknesses, but simulations and Gomperts's formula agree that for thicker barriers the frequencies of the minima in the sound insulation move to lower frequencies and vice versa.

According to the simulations and Gomperts's formula the width of the gap has only a much smaller influence on the frequencies of the minima. The gaps of the barrier at which the measurements have been performed had a different, more complicated geometry that did not allow a direct line of sight through the gap for all but the largest two measured gaps (see figure 3.6 for a cross section of the measured gap). Probably this special geometry is the reason for the observed grouping of gap widths that has already been discussed in chapter 5.1. Comparing the two parts of each pair in figure 5.1 shows that the first minima are always in the same frequency band, though the differences in the neighbouring frequency bands suggest that the frequency of the minimum is slightly lower for the larger gap of each pair. To check if this is really the case, the measurements have been analysed again, but this time the sound insulation has been calculated for single frequencies instead of third-octave bands. The results are plotted in figure 5.10 and show that with both pairs the minimum of sound insulation of the larger gap is at a slightly lower frequency than the minimum of the smaller gap. This fits well with the simulations and Gomperts's formula.

To find out the source of the minima in the *SI*, the following considerations have been made: The measurements, the simulations and Gomperts's formula all agree that for a barrier of thickness 12 cm there are minima in the sound insulation circa in the 1250 Hz and the 2500 Hz frequency bands. If the front and back of the gap reflected parts of the sound waves, the doubly reflected wave could interfere with the direct wave and resonances could occur. Using the thickness of the barrier as half a wavelength leads to a frequency of about 1430 Hz, which is higher than the first minimum. The impulse responses from the simulations discussed in chapter 4.4 showed peaks at intervals that suggest that reflections don't occur directly at the beginning and end of the gap but a little beyond. This extension of the sound path corresponds to the end correction that Gomperts used to account for the air directly in front of and directly behind the gap that is moved together with the air inside the gap. Hence the frequency at which interference

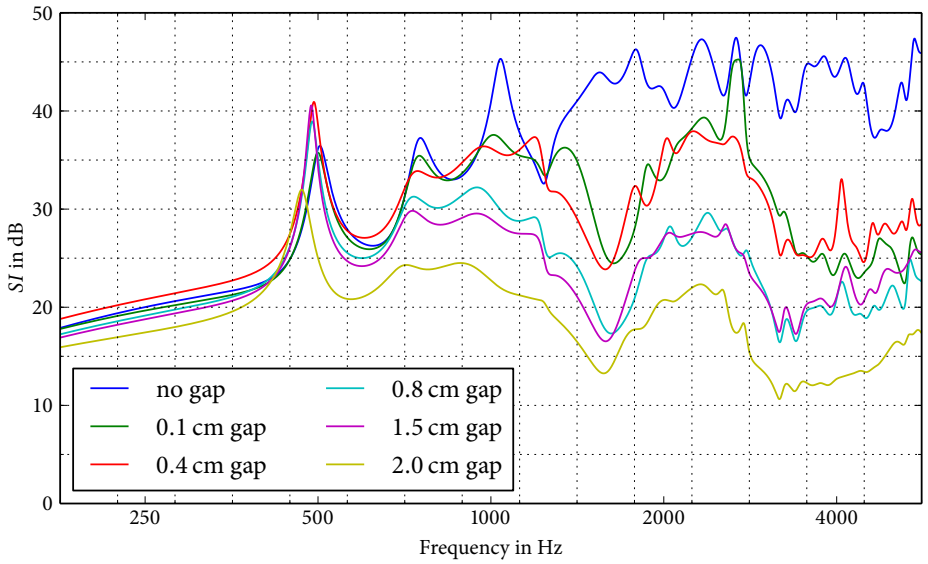

Figure 5.10: Measured sound insulation of noise barriers with gaps calculated for individual frequencies instead of third-octave bands (single-frequency sound insulation indices)

of the direct components through the gap and the components reflected at the back and front of the gap could occur is a little lower. Because the end correction and with it the distance of the imaginary reflection points from the end of the gap increase with the gap width, the resonance frequencies should be slightly lower for higher gap widths. This fits well with the movement of the frequencies of the minima observed with the BEM simulations and with Gomperts's formula and probably also with the measurements, though the influence of the different gap geometry is hard to quantify.

Comparing the results from the measurements with those from the simulations shows that the sound insulation of the measured barrier with gaps is significantly better than the sound insulation of the simulated barrier. Taking the single-number ratings from table 5.1 (measurements) and 5.2 (simulations) gives for instance for the measured 1.5 cm gap a $DL_{SI}^{400-4000\,\mathrm{Hz}}$ of 22.3 dB, but for both 2D and 3D simulations the sound insulation of a barrier with a (smaller, i.e. better insulating) gap of 1 cm is significantly worse; the $DL_{SI}^{400-4000\,\mathrm{Hz}}$ are less than 19 dB. The most likely reason for this large difference is the geometry of the gap: All simulated gaps are planar, but the gap in the measured barrier had a groove and a tongue (see figure 3.6), which reduced the visible cross section of the gap by the height of the tongue (1 cm). Therefore the measured results are shown together with simulated gaps of not the same width but of smaller width: Comparing the measured 1.5 cm gap with the simulated 0.5 cm gaps gives $DL_{SI}^{400-4000\,\mathrm{Hz}}$ that are closer to each other

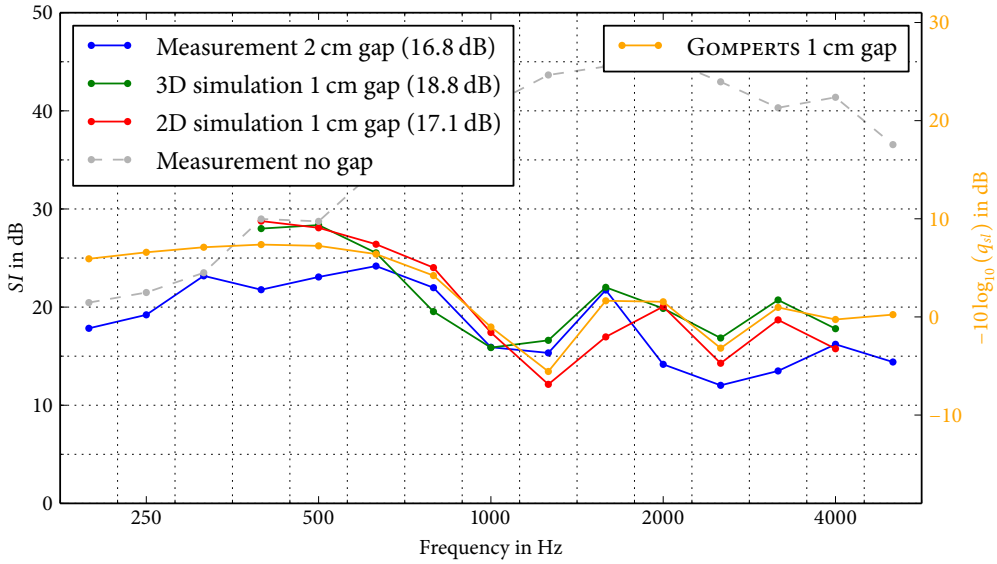

Figure 5.11: Sound insulation of noise barriers with 1–2 cm gaps. Comparison between measurement and simulations. Numbers in brackets in the legend are the single-number ratings $DL_{SI}^{400-4000\,\mathrm{Hz}}$

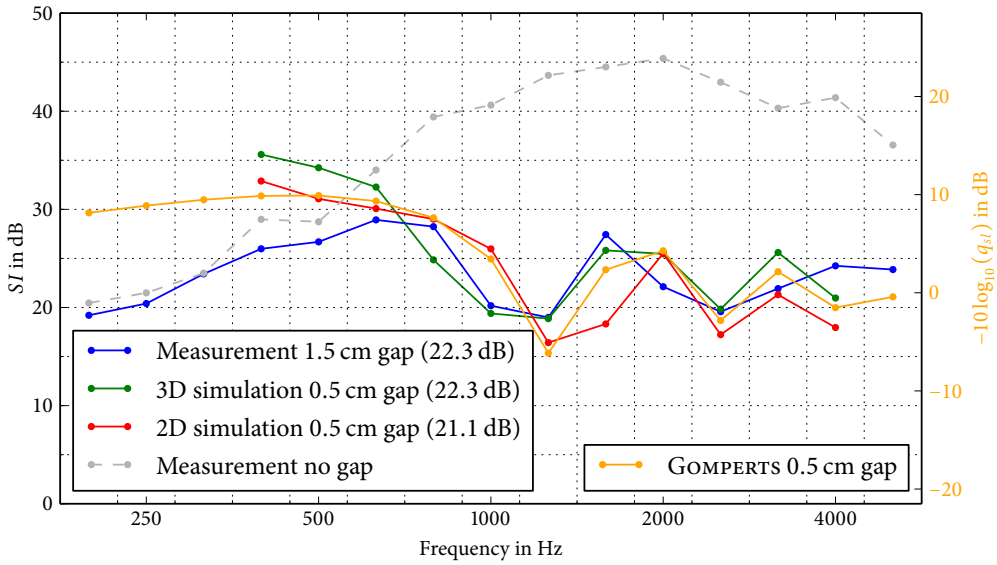

Figure 5.12: Sound insulation of noise barriers with 0.5–1.5 cm gaps. Comparison between measurement and simulations. Numbers in brackets in the legend are the single-number ratings $DL_{SI}^{400-4000\,\mathrm{Hz}}$

– that is 22.3 dB in the measurement and 21.1 dB (2D) respectively 22.3 dB (3D) in the simulation. The presentation of these unequal gap sizes together can thus be justified. Figure 5.11 shows the sound insulation indices of the measured 2 cm gap together with the two simulations for the 1 cm gap and figure 5.12 shows a similar comparison of the measured 1.5 cm gap with the simulated 0.5 cm gaps.

Still, simply subtracting the height of the tongue from the gap width does not lead to satisfying results in the remaining cases: For the measured gap widths of less than 1 cm, where there was no direct line of sight through the gap because of the tongue, a considerable amount of noise was still able to pass through the gap and the *SI* were therefore significantly reduced with respect to the gap-less barrier. It would be interesting to perform simulations of gaps with a groove and a tongue to study the impact of the geometry of the gap on the amount of sound leakage.

Both figure 5.11 and 5.12 show similar patterns: There are minima of the *SI* circa in the 1250 Hz band and the 2500 Hz band. Around the first minimum, i.e. from the 630 Hz band to the 1600 Hz band, there seem to be two different shapes: In both comparison figures the measurement and the 3D simulation have a broader minimum than the 2D simulation and Gomperts's formula. It could be that the source of these two different shapes is the difference in the propagation characteristics: The 2D simulation and Gomperts's formula assume cylindrical waves, whereas in the case of the 3D simulation spherical waves are used that better reflect the real, measured propagation characteristics.

Concerning the depth of the minima, the two simulations agree fairly well with each other and with Gomperts's formula. The depth of the minima from the measurements seems to be a little smaller though. There are two possible reasons for this: The first reason is that the sound insulation of the measured barrier with a gap is obviously limited by the sound insulation of the barrier itself with its perforated metal boxes filled with rock wool. This is especially evident for low frequencies, where the measured sound insulation is lower than the corresponding results from the BEM simulation and Gomperts's formula. To show this upper limit the measured sound insulation of the gap-less barrier was added to the two comparison figures. The simulated barriers do not have this upper limit for the sound insulation, because it was assumed that the surface of the barrier is fully reflective and that sound can only pass through the gap and not through the barrier itself.

The second possible reason for the difference in the depth of the minima between measurements and simulations could be the difference in the gap width. Looking for example at the four simulated gap widths in figure 5.2, one can see that with increasing gap widths not only the DL_{SI} decreases, but also the depths of the minima become smaller. It could be that the complicated cross section of the measured 2 cm gap makes it similar to the simulated planar 1 cm gaps only in the single-number rating DL_{SI}, but does not equally change the depth of the minima of the *SI*. Again, simulations of gaps with a groove and a

tongue could shed some light on which parts of the discrepancy between measurements and simulations originate from the different geometries of the gaps.

5.5 Directivity

The following pages contain a number of figures that illustrate the radiation pattern of the gaps. Figures 5.13 and 5.15 to 5.23 show the single-frequency sound insulation indices; that means that the plotted values are the logarithm of the ratio of the energy in the impulse response with the barrier to the energy in the free-field impulse response. The only difference to the third-octave frequency band sound insulation indices SI given earlier in this thesis is that for the single-frequency values the ratio has been calculated for each frequency individually, whereas the method used earlier compares the total energy in all frequencies within a certain third-octave band as specified by the standard EN 1793-6.

The top of the figures shows a contour plot of the single-frequency sound insulation indices. The frequencies are plotted on the abscissa, and the ordinate shows the position of the microphone relative to the gap in cm. The bottom of the figures plots the single-frequency sound insulation indices averaged over all microphone positions shown in the top of the figure (continuous line). For comparison, the single-frequency sound insulation indices for the two microphones directly behind the gap (dashed line) and 40 cm above the gap (dotted line) are also plotted individually.

Figures 5.13 and 5.14 show the results for the measured 2 cm gap in the 12 cm barrier. In contrast to the simulations shown in the following figures, with the measured barrier sound can leak not only through the gap but also through the noise barrier itself. Figure 5.14 shows the attempt to visualise only the sound transmitted through the gap by comparing the energy in the impulse response with the gap to the energy in the impulse response of the gap-less barrier instead of the energy in the free-field impulse response.

Figure 5.15 shows the results for the 1 cm gap in the 12 cm barrier from the 2D simulation. The upper half of the contour plot was calculated with a mesh density of 18 nodes per wavelength, and the lower half of the contour plot was calculated for the same barrier but with a mesh density of 6 nodes per wavelength. For most frequencies, the difference between the two meshes is not large enough to justify the substantial increase of the computation time for the denser mesh.

The changes for the single-frequency sound insulation indices from the 3D simulations are shown in figures 5.16 to 5.19 for 0.5 cm to 5 cm gaps in 12 cm barriers, and in figures 5.20 and 5.21 for 1 cm gaps in 8 cm and 16 cm barriers.

For the 0.5 cm gap in the 12 cm barrier (figure 5.16) there are three minima: The first minimum is located at a frequency of circa 1200 Hz and exists for all microphone positions, but for those microphone positions further away from the gap it is a bit less pronounced – the difference between the minimum sound insulation for the centre microphone and for the microphone 40 cm above is about 6 dB. The second minimum is around the 2500 Hz frequency and has a slightly different shape: Regarding the different vertical microphone positions there is one minimum at the centre position and two symmetric minima are circa 30 cm above and below the gap. For the third minimum at around 3800 Hz it is harder to judge the shape of the contour lines, because for the higher frequencies the sound insulation is not so smooth any more and the contour lines contain a lot of zig-zag-patterns. The author considers it possible that these uneven shapes are the result of the rather coarse meshes used for the simulations in order to keep the computing time acceptable. A small unevenness does not exert a large influence on the sound insulation indices *SI* discussed in the previous chapters, because the sound insulation indices take the average over full third octave bands, but the contour graphs shown here make the unevenness very well visible. Around the 3000 Hz frequency there are a few spikes for the relative microphone positions of ±30 cm where the sound insulation locally increases for more than 30 dB. Again, the author assumes that these are errors that stem from the used meshes and not the result of physical effects. It would be interesting to perform additional simulations for the very same barrier gap dimensions but with a finer mesh to see how much influence the density of the mesh has on the spatial changes of the sound insulation. (In fact, two simulations of the same barrier gap combination have been performed in 2D and the results are shown in figure 5.15, but in that case even the wider, i.e. worse, mesh does not exhibit comparable spikes in the sound insulation.)

Figure 5.17 shows the results from the 1 cm gap in the 12 cm barrier and has a rather similar pattern: There are three minima at nearly the same, only (as expected) marginally lower frequencies. The peaks around 3000 Hz are not as prominent, but there are new spikes close to 5000 Hz. In comparison, figure 5.18 (2 cm gap in the 12 cm barrier) looks rather different: There are a number of spikes at many frequencies for the microphone positions more than 20 cm above or below the gap and the minima in the sound insulation are less pronounced. Finally, the widest gap, i.e. the 5 cm gap in the 12 cm barrier (figure 5.19), again gives a different view: There are no strange spikes, but the sound insulation is so low for most frequencies and microphone positions that the difference in the sound insulation between the minima and the maxima is rather small.

Figure 5.20 shows the case of a thinner barrier: With the 1 cm gap in the 8 cm barrier there are two main minima, one at circa 1500 Hz and one at circa 3500 Hz, but the first minimum has a side minimum directly attached at circa 2000 Hz. For higher frequencies starting around 3000 Hz the contour lines become ragged again.

The results for a barrier of increased thickness are presented in figure 5.21: With the 1 cm

gap in the 16 cm barrier there are five large minima. The first minimum at about 800 Hz is smooth over all microphone positions, the second minimum at circa 1900 Hz again has one main minimum at the centre microphone position and two symmetric minima at the microphone positions circa 30 cm above and below the gap. For the next three minima up to the minimum at circa 5000 Hz again the raggedness makes it harder to judge the shape of the minima.

The last two figures rotate the displayed plane and show the changes of the sound insulation indices along a line parallel to the gap: Figure 5.22 shows the results for the microphone directly behind the gap and figure 5.23 shows the same results but for microphones 40 cm above the gap. In comparison to the changes perpendicular to the gap the changes of the sound insulation parallel to the gap are insignificant.

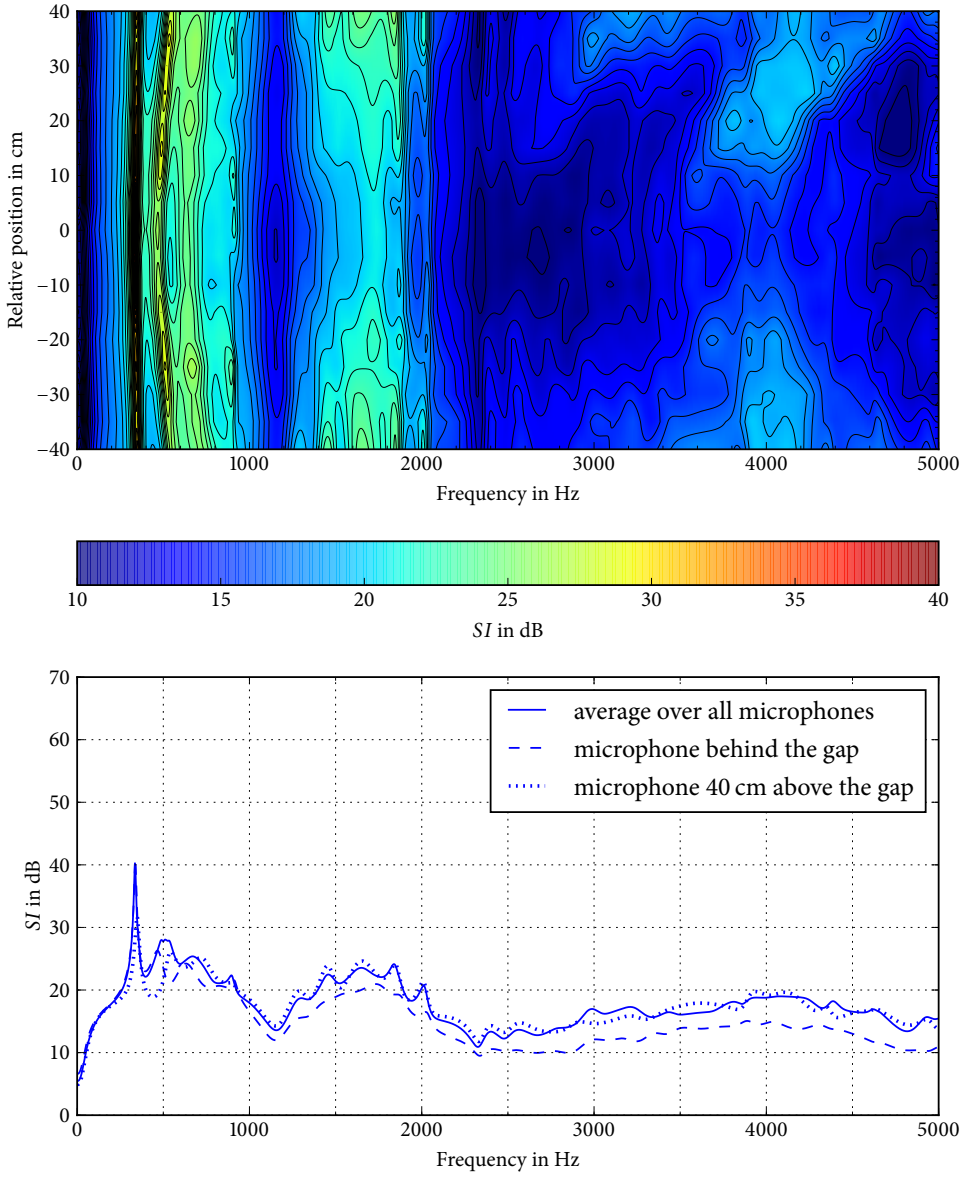

Figure 5.13: Change of the single-frequency sound insulation indices with the vertical position for the **2 cm gap from the measurement**. Top: Contour plot with the vertical position of the microphone relative to the gap plotted on the ordinate. Bottom: Average over all microphone positions shown above and two microphones individually for comparison

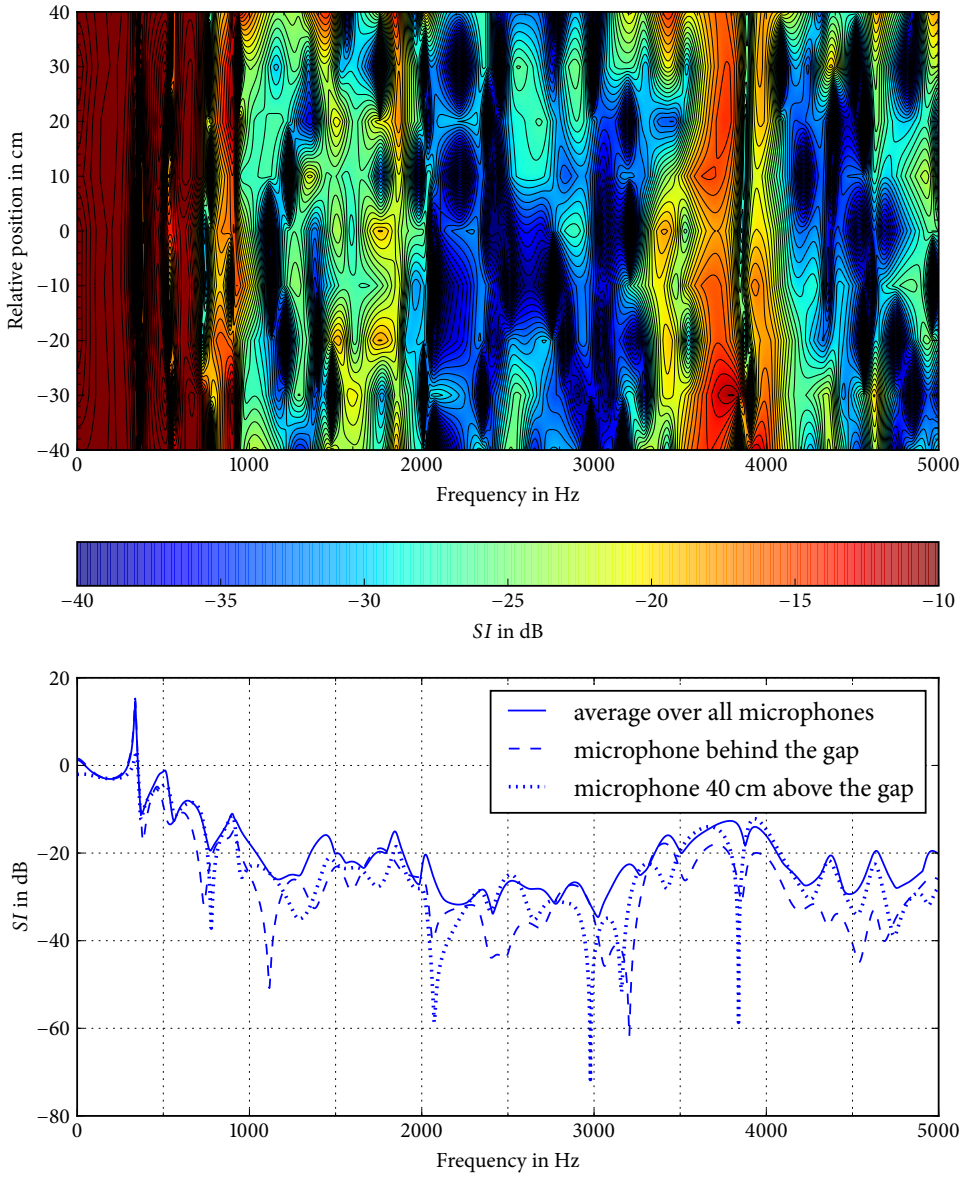

Figure 5.14: Change of the single-frequency sound insulation indices, **relative to the energy measured at the gap-less barrier** instead of the free-field energy with the vertical position for the **2 cm gap from the measurement**. Top: Contour plot with the vertical position of the microphone relative to the gap plotted on the ordinate. Bottom: Average over all microphone positions shown above and two microphones individually for comparison

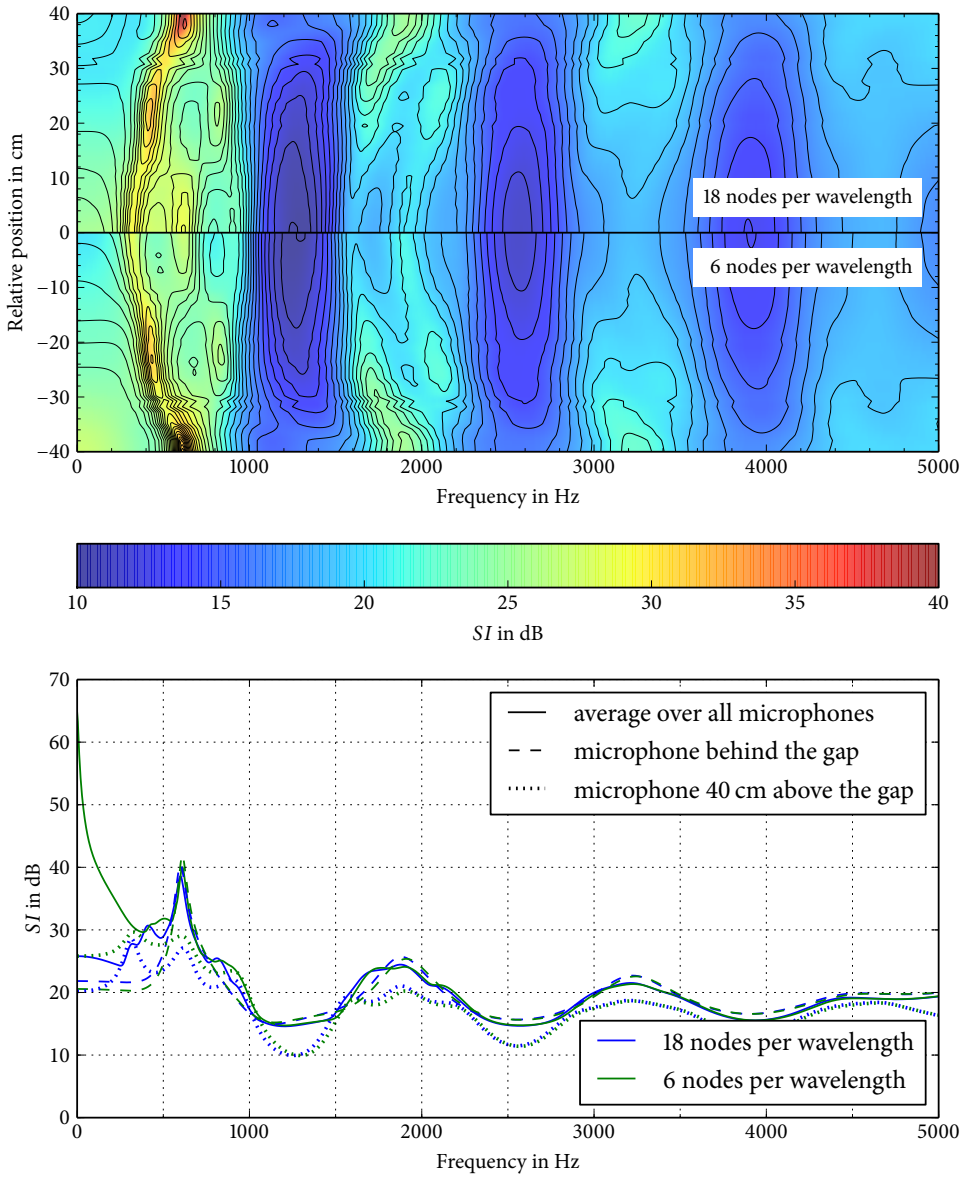

Figure 5.15: Change of the single-frequency sound insulation indices with the vertical position for the **1 cm gap in the 12 cm barrier from the 2D simulation**. Top: Contour plot with the vertical position of the microphone relative to the gap plotted on the ordinate. The upper half shows the results for a mesh density of 18 nodes per wavelength, whereas the lower half shows the result for a mesh density of 6 nodes per wavelength. Bottom: Average over all microphone positions shown above and two microphones individually for comparison.

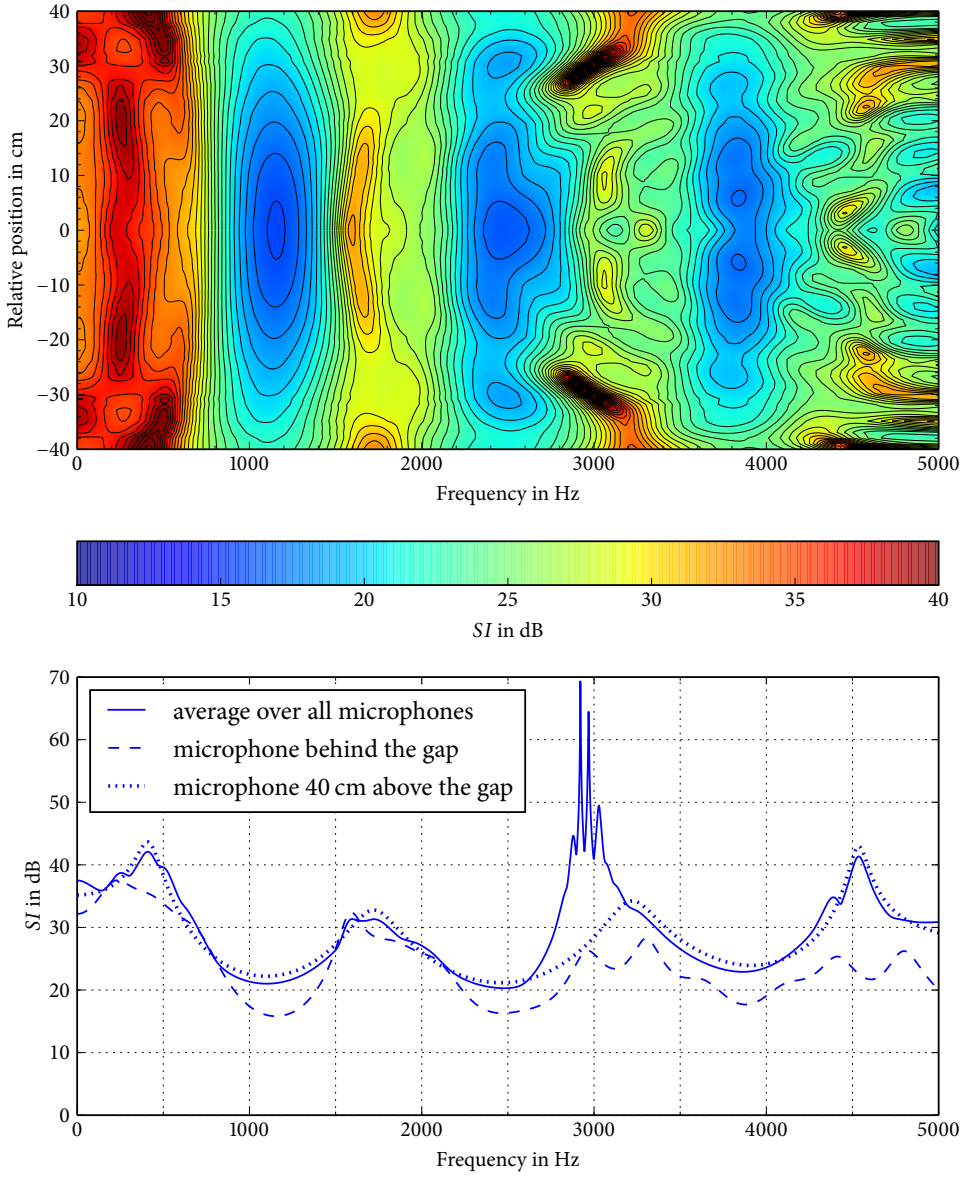

Figure 5.16: Change of the single-frequency sound insulation indices with the vertical position for the **0.5 cm gap in the 12 cm barrier from the 3D simulation**. Top: Contour plot with the vertical position of the microphone relative to the gap plotted on the ordinate. Bottom: Average over all microphone positions shown above and two microphones individually for comparison

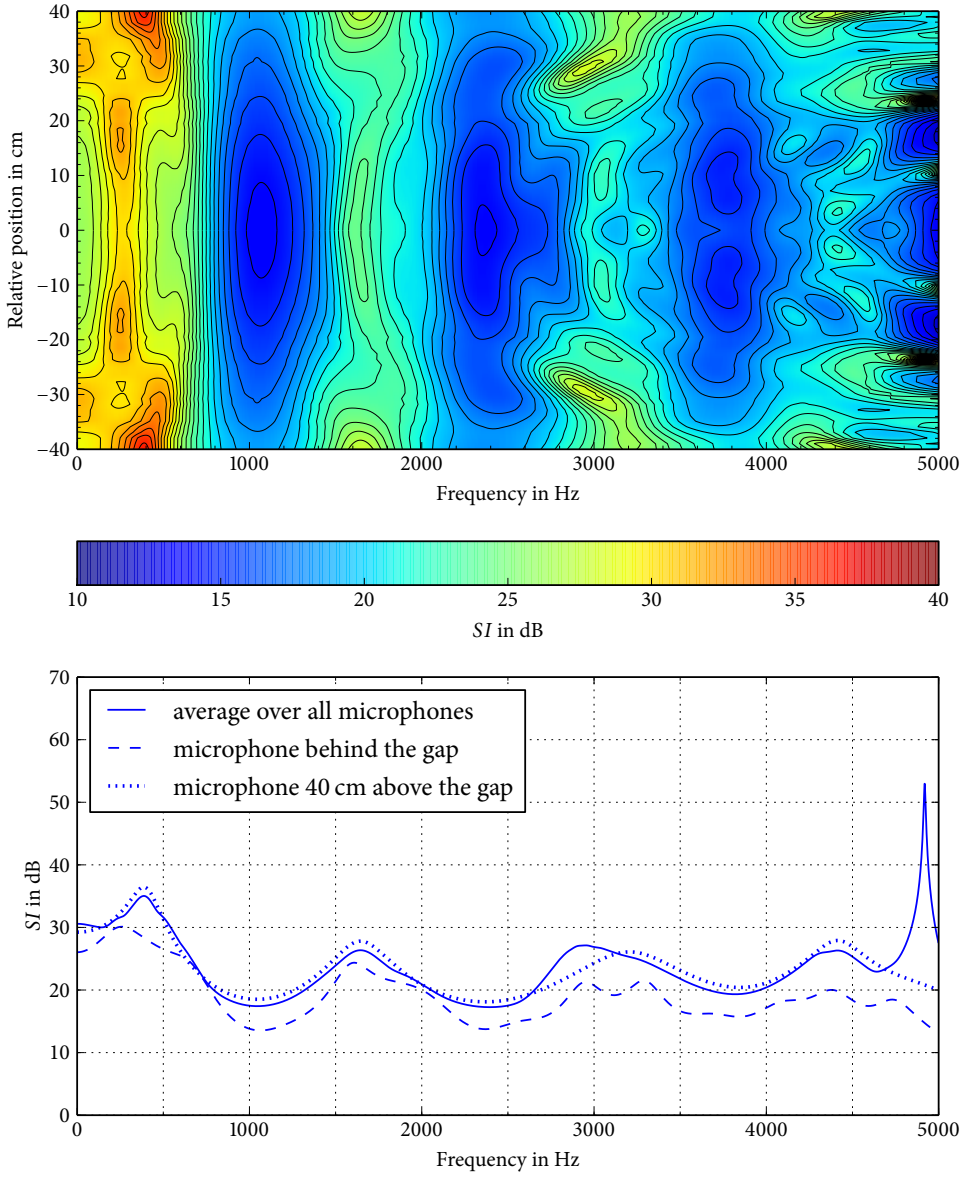

Figure 5.17: Change of the single-frequency sound insulation indices with the vertical position for the **1 cm gap in the 12 cm barrier from the 3D simulation**. Top: Contour plot with the vertical position of the microphone relative to the gap plotted on the ordinate. Bottom: Average over all microphone positions shown above and two microphones individually for comparison

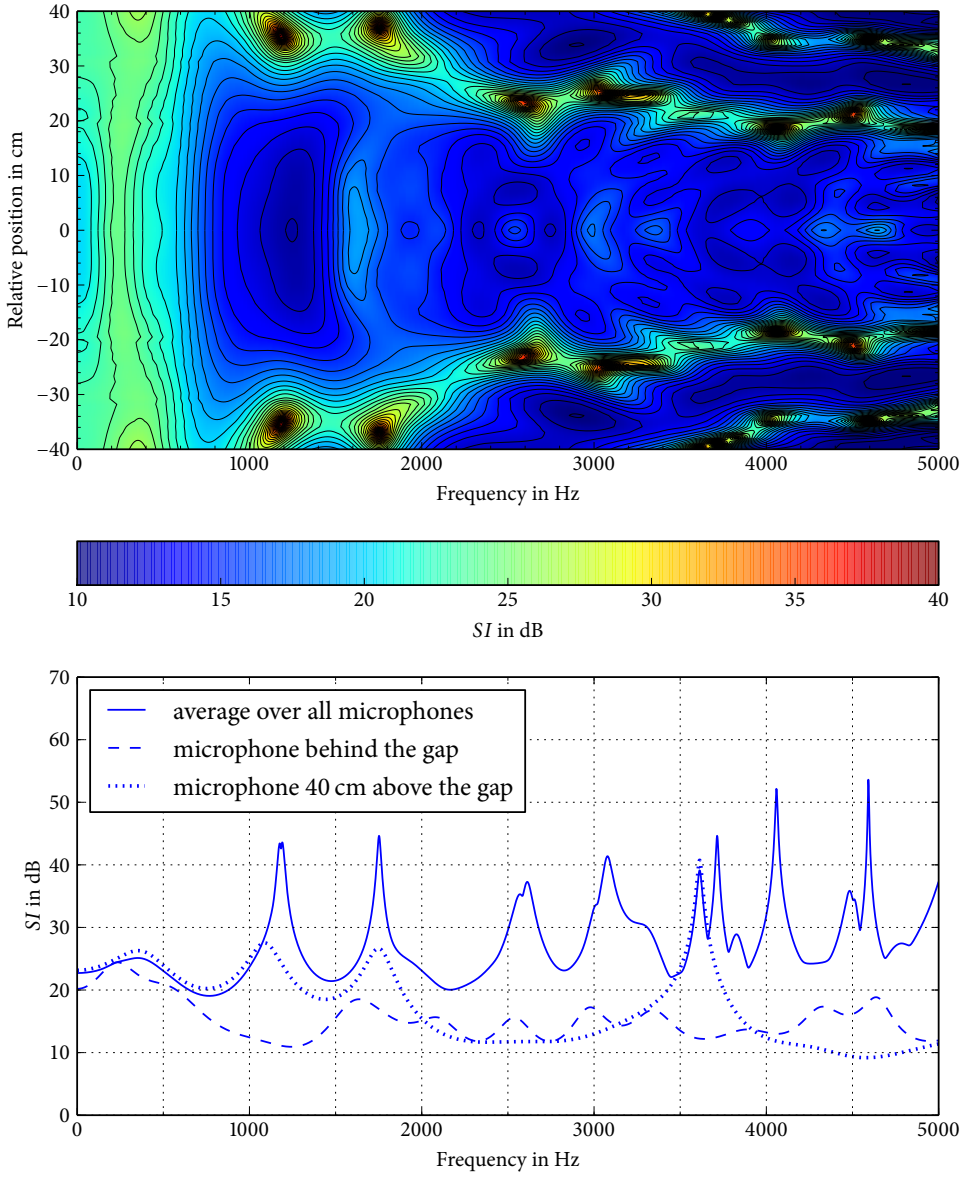

Figure 5.18: Change of the single-frequency sound insulation indices with the vertical position for the **2 cm gap in the 12 cm barrier from the 3D simulation**. Top: Contour plot with the vertical position of the microphone relative to the gap plotted on the ordinate. Bottom: Average over all microphone positions shown above and two microphones individually for comparison

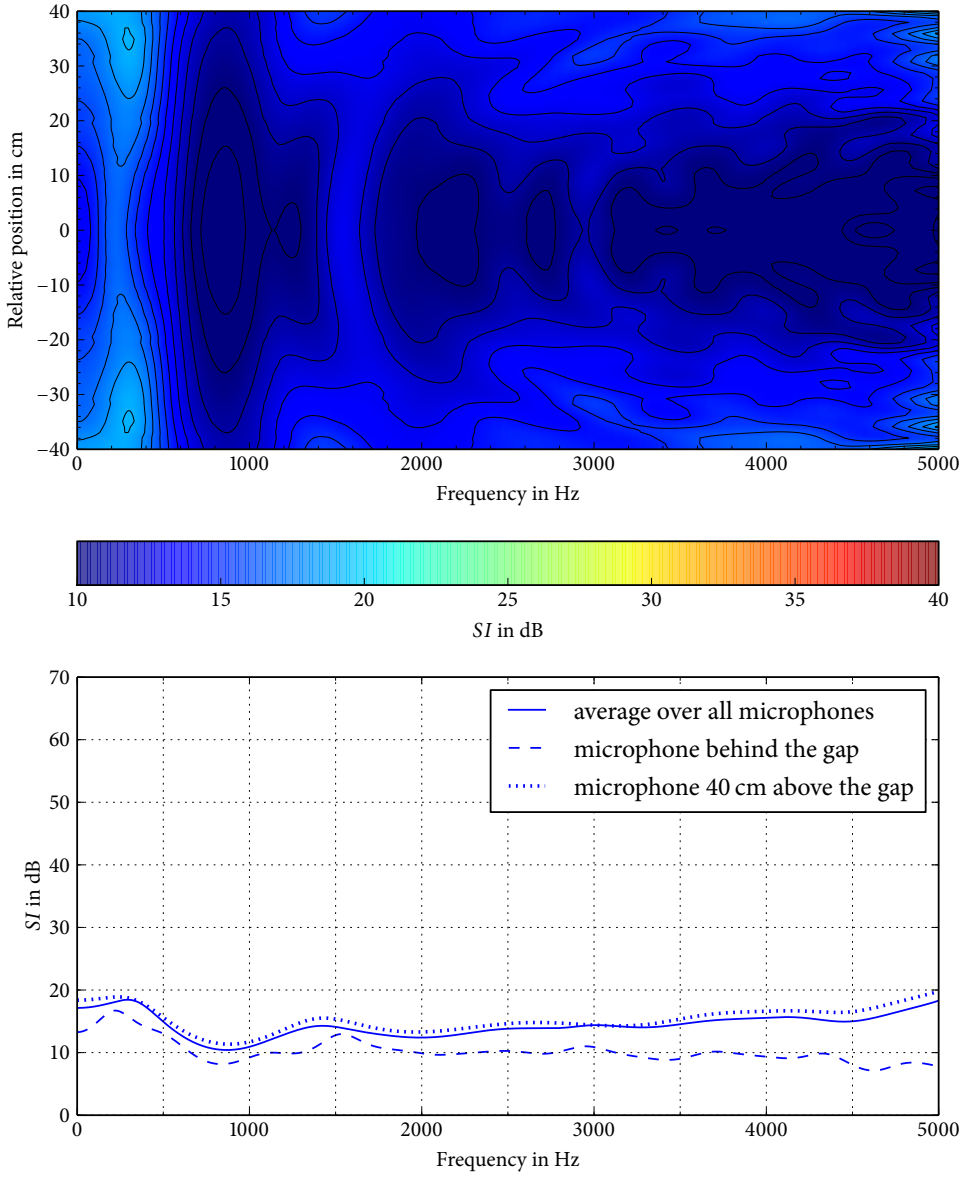

Figure 5.19: Change of the single-frequency sound insulation indices with the vertical position for the **5 cm gap in the 12 cm barrier from the 3D simulation**. Top: Contour plot with the vertical position of the microphone relative to the gap plotted on the ordinate. Bottom: Average over all microphone positions shown above and two microphones individually for comparison

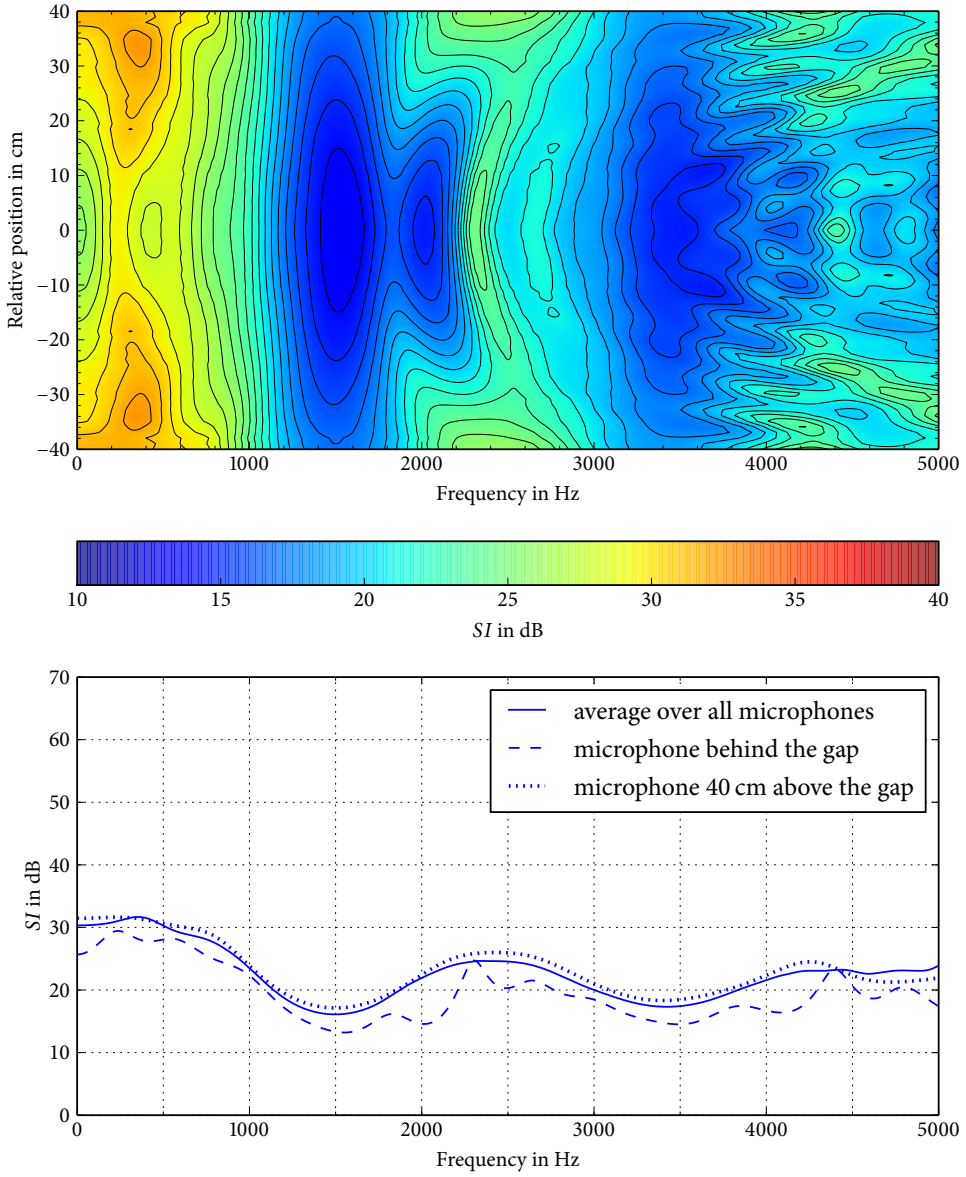

Figure 5.20: Change of the single-frequency sound insulation indices with the vertical position for the **1 cm gap in the 8 cm barrier from the 3D simulation**. Top: Contour plot with the vertical position of the microphone relative to the gap plotted on the ordinate. Bottom: Average over all microphone positions shown above and two microphones individually for comparison

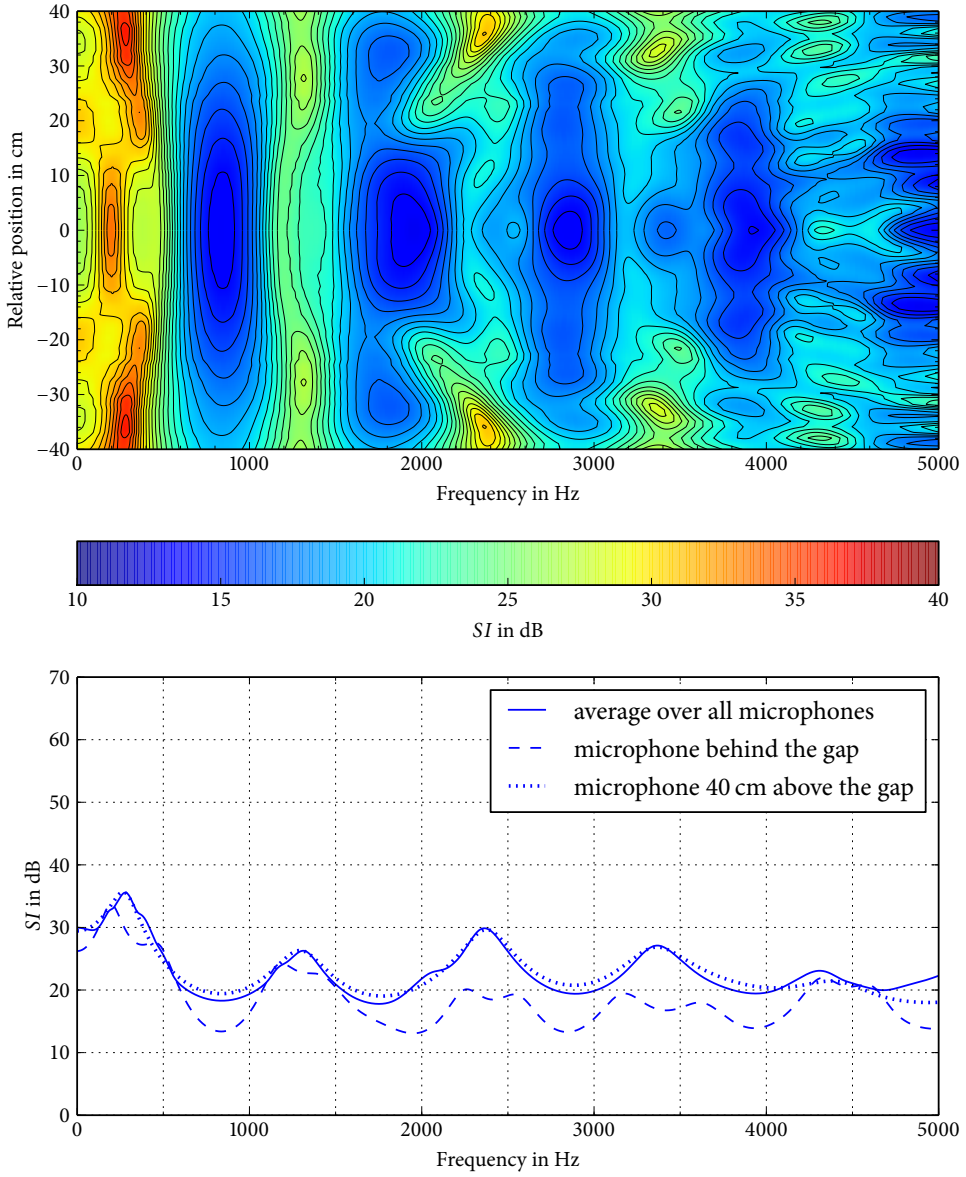

Figure 5.21: Change of the single-frequency sound insulation indices with the vertical position for the **1 cm gap in the 16 cm barrier from the 3D simulation**. Top: Contour plot with the vertical position of the microphone relative to the gap plotted on the ordinate. Bottom: Average over all microphone positions shown above and two microphones individually for comparison

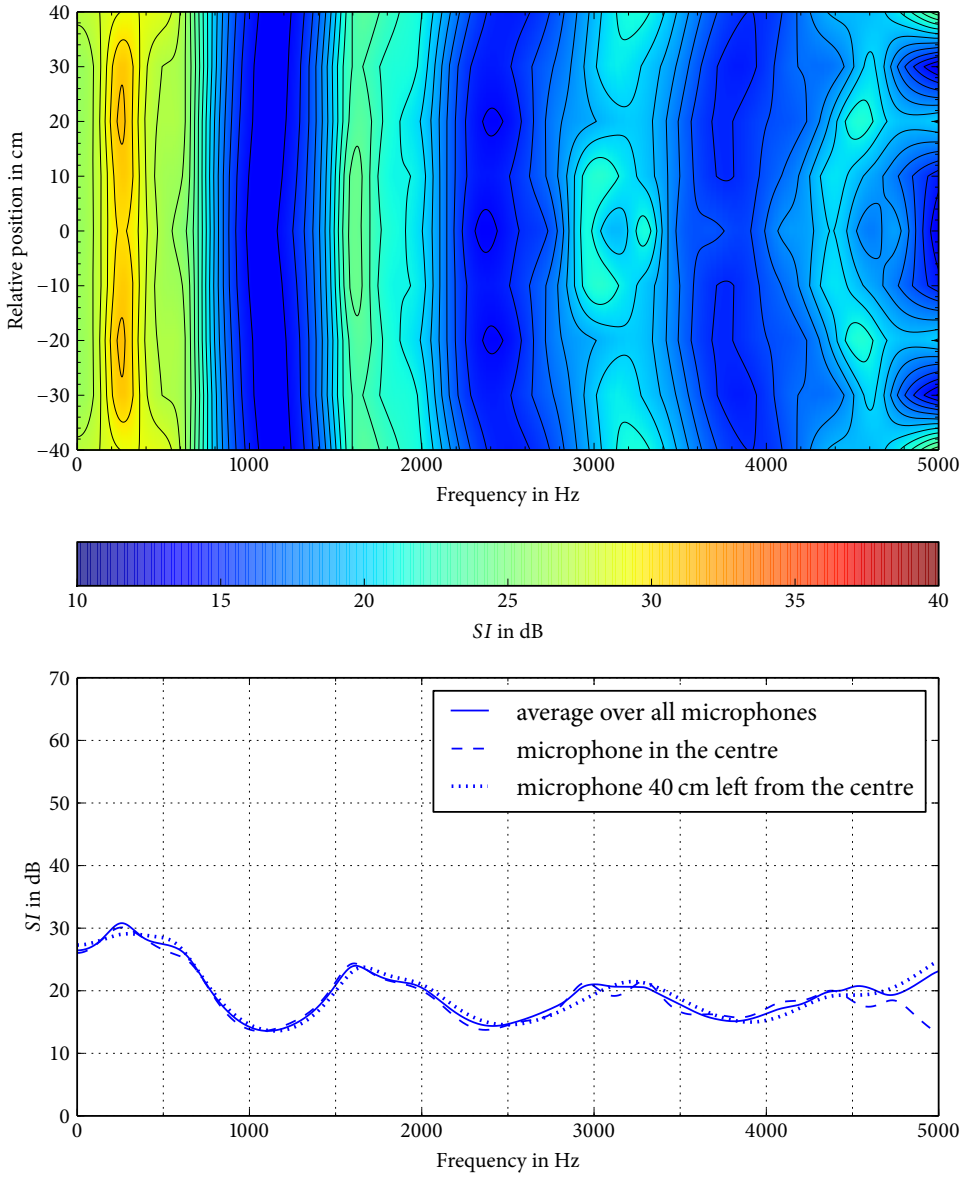

Figure 5.22: Change of the single-frequency sound insulation indices with the **horizontal** position for the 1 cm gap in the 12 cm barrier from the 3D simulation with the **same vertical position as the gap**. Top: Contour plot with the vertical position of the microphone relative to the gap plotted on the ordinate. Bottom: Average over all microphone positions shown above and two microphones individually for comparison

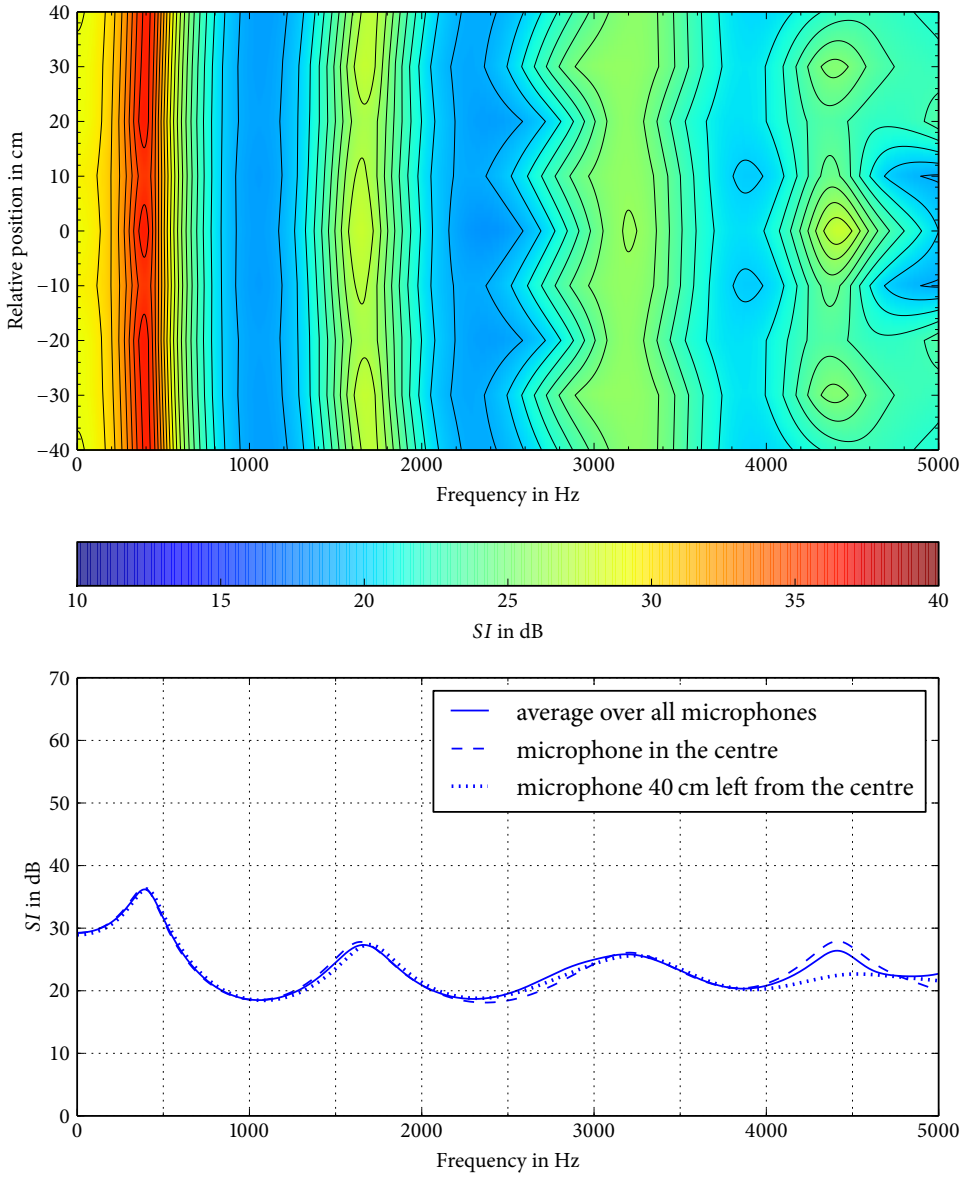

Figure 5.23: Change of the single-frequency sound insulation indices with the **horizontal** position for the 1 cm gap in the 12 cm barrier from the 3D simulation with the **vertical position 40 cm above the gap**. Top: Contour plot with the vertical position of the microphone relative to the gap plotted on the ordinate. Bottom: Average over all microphone positions shown above and two microphones individually for comparison

5.6 Improvements to the Simulation Method

There are a number of different gap shapes that should be studied further: On the one hand it would be great if measurements of a planar gap could be performed. On the other hand it would be interesting to study the effect of the groove and the tongue in the gap with the help of simulations. Unfortunately, modelling a groove and a tongue in 3D means that one of the symmetry planes disappears, thereby significantly increasing the necessary computation time.

The author wants to present an idea on how the simulations in this thesis could be improved and sped up: After the simulations performed for this thesis were finished, the author tried to find out if it would be possible to get smoother results from 3D simulations than those shown in figure 4.4 with the help of a faster computer[1]. The computation time of the calculations performed for this thesis was kept to reasonable levels by two decisions: Firstly, different meshes were used for lower frequencies to keep the number of surface panels as low as possible, and secondly, the CHIEF technique was not used to solve the non-uniqueness problem. This second choice was reviewed during the reconsiderations: A small noise barrier was simulated with CHIEF points. While the use of CHIEF points removed some of the "noise" from the impulse response, even a very large number of randomly chosen CHIEF points (four times the number of calculated surface elements, so that if the symmetry is ignored, the number of CHIEF points is equal to the number of surface elements) did not produce perfectly smooth results. The reason for this was that with each change of the mesh, the calculated sound pressure at the microphone positions jumped far enough that the impulse responses still contained the "noise". (One attempt with a higher mesh density of 14 nodes per wavelength still did not deliver the desired results.) Finally, a smooth pressure curve and a good-looking impulse response were achieved for at least 0-2000 Hz by using the large number of CHIEF points and the same mesh for every frequency. Still, using the same mesh for all frequencies up to 5000 Hz is not a viable option because of the computation time.

The author therefore would like to propose the following idea: Calculating the impulse response with the help of the FFT from sound pressure values at linearly-spaced frequencies as done in this thesis brings about that for higher frequency bands a larger number of BEM calculations have to be performed than for lower frequency bands. For a frequency spacing of 2 Hz, the 4000 Hz band contains 459 frequencies for which the BEM calculation

[1] When most of the simulations performed for this thesis had been done, a faster computing server was made available for acoustic simulations. This new computer not only increased the number of processor cores and their clock frequency, but the new processors support a newer instruction set that can perform floating point operations on twice as many numbers as was previously possible in the same time (256 bit vector operations with AVX instead of 128 bit operations with the older SSE instructions). The 3-4x increased computing power of the new server made the following considerations possible.

has to be performed, whereas there are only 46 equivalent frequencies in the 400 Hz band. Fortunately, most of the Adrienne analysis is performed in third octave frequency bands anyway. It might therefore be possible to take for every frequency band for instance 100 equally spaced frequencies between the lower limit frequency and the upper limit frequency and then calculate a separate impulse response for every frequency band from this data, thereby setting the sound pressure for all lower and higher frequencies to zero. The subsequent calculations have to be performed always on the fitting impulse responses. This strategy has the advantage that it would be viable to use the same mesh for all frequencies within a band, thereby avoiding the other of the two reasons for the "noise" in the impulse response.

6 Summary

In this thesis the impact of gaps on the in situ airborne sound insulation of noise barriers has been examined. With the help of wedges, gaps have been produced in a barrier and the sound insulation has been measured in accordance to EN 1793-6. Computer simulations of similar gaps have been carried out using the boundary element method. Besides, the results have been compared to analytical calculations by Gomperts [14].

The following observations have been made:

- The sound insulation varies significantly across the different frequency bands, yet the minima occur at the same frequency bands for both the measurements and the simulations for comparable barrier and gap dimensions. A strong correlation between the positions of the minima and the thickness of the barrier and thus the length of the gap has been shown. The width of the gap only has a small influence on the positions of the minima, but is strongly associated with the overall decrease of the sound insulation.
- The measured sound insulation is a bit higher than the simulated one. One reason for this difference is that the groove and tongue from the measured barrier have not been reproduced in the simulation in order to maintain a symmetry plane that helped avoid unreasonable computation times.
- The measurements show that even a gap of only 0.1 cm significantly reduces the sound insulation especially at higher frequencies.

In conclusion, it can be said that a significant amount of noise can be transmitted through construction faults. To reach high sound insulation values it is therefore necessary to exercise care in the assembly of noise barriers.

List of Figures

List of Tables

Bibliography

[1] Müller, Gerhard (Ed.) ; Möser, Michael (Ed.): *Handbook of Engineering Acoustics*. Springer, 2013

[2] Möser, Michael ; Zimmermann, Stefan ; Ellis, Rebecca: *Engineering Acoustics*. Springer, 2009

[3] Lerch, Gerhard ; Sessler, Gerhard ; Wolf, Dietrich: *Technische Akustik*. Springer, 2009

[4] Weinzierl, Stefan (Ed.): *Handbuch der Audiotechnik*. Springer, 2008

[5] Ciskowski, Robert D. (Ed.) ; Brebbia, Carlos A. (Ed.): *Boundary Element Methods in Acoustics*. Springer, 1991

[6] Iemma, Umberto ; Marchese, Vincenzo: *AcouSTO 1.5 User Manual*. 2013

[7] Kirkup, Stephen: *The Boundary Element Method in Acoustics*. 2007 `http://boundary-element-method.com`

[8] Juhl, Peter M.: *The Boundary Element Method for Sound Field Calculations*, Technical University of Denmark, Doctoral Thesis, 1993

[9] Cutanda Henríquez, Vicente: *Numerical Transducer Modeling*, Technical University of Denmark, Doctoral Thesis, 2002

[10] Alpera, Susana Quirós y. ; Jacobsen, Finn ; Juhl, Peter M. ; Cutanda Henríquez, Vicente: A BEM approach to validate a model for predicting sound propagation over non-flat terrain. In: *Applied Acoustics* 64 (2003), p. 781

[11] Cutanda Henríquez, Vicente ; Juhl, Peter M.: OpenBEM – An open source Boundary Element Method software in Acoustics. In: *Proceedings of Inter-Noise 2010, Lisbon, Portugal*

[12] Schenck, Harry A.: Improved Integral Formulation for Acoustic Radiation Problems. In: *Journal of the Acoustical Society of America* 44 (1968), p. 41

[13] Smits, J. M. A. ; Kosten, C. W.: Sound absorption by slit resonators. In: *Acustica* 1 (1951), p. 114

[14] Gomperts, M. C.: The "Sound Insulation" of Circular and Slit-shaped Apertures. In: *Acustica* 14 (1964), p. 1

[15] Gomperts, M. C. ; Kihlman, T.: The Sound Transmission Loss of Circular and Slit-Shaped Apertures in Walls. In: *Acustica* 18 (1967), p. 144

[16] *QUIESST Guidebook to Noise Reducing Devices optimisation*. 2012 http://www.quiesst.eu/images/stories/guidebook_JPC_19_nov_2012_MC_CD_MG_logos.pdf

[17] Wehr, Reinhard: *In-Situ-Bewertung der akustischen Eigenschaften von Lärmschutzeinrichtungen an Verkehrswegen*, Vienna University of Technology, Master Thesis, 2011

[18] Iemma, Umberto ; Marchese, Vincenzo: *AcouSTO*. http://acousto.sf.net

[19] Juhl, Peter M. ; Cutanda Henríquez, Vicente: *OpenBEM*. http://openbem.dk

[20] *OpenMPI. A High Performance Message Passing Library*. http://open-mpi.org

[21] *ATLAS. Automatically Tuned Linear Algebra Software*. http://math-atlas.sf.net

[22] The MathWorks, Inc.: *Matlab*. http://mathworks.com/products/matlab

[23] *Python. A programming language*. http://python.org

[24] *SciPy. Open source scientific tools for Python*. http://scipy.org

[25] European Committee for Standardization: *EN 1793-2 Road traffic noise reducing devices – Test method for determining the acoustic performance – Part 2: Intrinsic characteristics of airborne sound insulation under diffuse sound field conditions*. 2013

[26] European Committee for Standardization: *EN 1793-3 Road traffic noise reducing devices – Test method for determining the acoustic performance – Part 3: Normalized traffic noise spectrum*. 1997

[27] European Committee for Standardization: *EN 1793-6 Road traffic noise reducing devices – Test method for determining the acoustic performance – Part 6: Intrinsic characteristics – In situ values of airborne sound insulation under direct sound field conditions*. 2013

[28] European Committee for Standardization: *EN ISO 10140-2 Acoustics – Laboratory measurement of sound insulation of building elements – Part 2: Measurement of airborne sound insulation*. 2010

[29] European Committee for Standardization: *EN ISO 18233 Acoustics – Application of new measurement methods in building and room acoustics*. 2006

[30] International Electrotechnical Commission: *IEC 61672-1 Electroacoustics – Sound level meters – Part 1: Specifications*. 2002